Facultad de Ciencias

DOS APROXIMACIONES A LA COSMOLOGÍA OBSERVACIONAL MODERNA: DETECCIÓN DE FUENTES PUNTUALES EN MAPAS DE LA POLARIZACIÓN DEL FONDO CÓSMICO DE MICROONDAS Y ESTIMACIÓN DE LA DISTRIBUCIÓN DE MATERIA OSCURA EN CÚMULOS DE GALAXIAS

Two Approaches to Modern Observational Cosmology: Detection of Point-like Sources in Polarization Maps of the Cosmic Microwave Background, and Estimation of Dark Matter Distribution in Galaxy Clusters

Trabajo de Fin de Grado
para acceder al

GRADO EN FÍSICA

Autora: Patricia Diego Palazuelos

Director: Patricio Vielva Martínez

Co-Director: Ian Dell'Antonio

Septiembre 2018

To my family and friends,
who may know nothing about the infinitude of space,
but are well acquainted with my infinite stupidity.

Abstract

In this work, two of the current researching fields in Modern Observational Cosmology are approached: the search for observational evidence of primordial gravitational waves, and the determination of the properties of dark matter. Firstly, a wavelet-based filter was designed to characterize the properties of the extragalactic point-like sources which threaten to obscure the signal left by primordial gravitational waves in the Cosmic Microwave Background. Tests of the filter performance in simulations of the microwave sky show the advantages of operating in E- and B-mode polarization maps, particularly in the B-mode, rather than in the maps of the conventional Stokes' parameters Q and U, when working with point-like sources. Secondly, the basics behind Weak Gravitational Lensing techniques are also reviewed, applying them to map the projected mass density of the A2142 Abell galaxy cluster. The combination of maps of projected mass density, like the ones constructed here with the galaxies distribution seen on mergers of galaxy clusters, could lead to new constrains on the physical properties of dark matter, like its self-interactions.

KEYWORDS: Cosmic Microwave Background, Inflation, Point-like Source Detection, Dark Matter, Weak Gravitational Lensing

Resumen

En este trabajo se tratan dos de las líneas de investigación que actualmente ocupan a la Cosmología Observacional Moderna: la búsqueda de pruebas observacionales de las ondas gravitacionales primigéneas y la determinación de las propiedades de la materia oscura. En relación al primer aspecto, se ha diseñado un filtro para caracterizar las propiedades de las fuentes puntuales extragalácticas, las cuales amenazan con ocultar la señal dejada por las ondas gravitacionales primigéneas en el Fondo Cósmico de Microondas. Las pruebas realizadas con el nuevo filtro usando simulaciones del cielo de microondas, demuestran las ventajas que a la hora de trabajar con fuentes puntuales implica operar en mapas de los modos E y B de polarización, especialmente en el modo B, en lugar de usar los convencionales mapas de los parámetros de Stokes Q y U. En lo que al segundo tema se refiere, se revisan los fundamentos detrás del efecto Lente Gravitacional Débil, aplicandolos al mapeado de la densidad de masa proyectada del cúmulo de galaxias A2142. Combinando mapas de densidad de masa proyectada como los aquí obtenidos, con la distribución de galaxias que puede observarse en colisiones de cúmulos galácticos, pueden acotarse propiedades físicas de la materia oscura, como su capacidad de auto-interacción.

PALABRAS CLAVE: Fondo Cósmico de Microondas, Inflación, Detección de Fuentes Puntuales, Materia Oscura, Efecto Lente Gravitacional Débil

Foreword

The work presented in this Final Degree Project was done between the *Observational Cosmology and Instrumentation Group* of the Instituto de Física de Cantabria (IFCA) and the *Gravitational Lensing Group* at the Physics Department of Brown University. Due to this dual nature, the work entwines two sharply differentiated researching fields nevertheless bound together by the current state of Observational Cosmology. The research I carried is related to two unsolved questions of Modern Cosmology: the search for observational proof of cosmic inflation, and the characterization of Dark Matter (DM) distribution and properties.

Since the beginning of my Physics Degree, and even before though I never admitted it out loud, I had my eyes on astronomy. So when the time came, I didn't have a doubt I would do my Final Degree Project on astrophysics. Finally, I chose to work with Professor Patricio Vielva on point-like source detection on E- and B-mode CMB maps, a choice I've never regretted once. The project's goal was to design a filter, based on the steerable wavelet philosophy, to determine the two quantities that characterize the source: the polarization angle and intensity. The application here explored was done on sources of known position, but due to its properties, I'm quite confident that it could easily be used on a *blind detection* scheme to actually detect and catalog the sources on polarization maps as well. This first part of this Final Degree Project was done in the frame of a *Beca de Colaboración del Ministerio de Educación, Cultura y Deporte* at the Departamento de Física Moderna of the Universidad de Cantabria.

In early November, the Facultad de Ciencias of the Universidad de Cantabria also gave me the amazing opportunity to participate in a summer student program at Brown University to extend my Final Degree Project, for which I'm deeply grateful. There, I joined the *Gravitational Lensing Group* for a two-month research visit and took part of the early stages of their new project to map the DM distribution of around 400 galaxy clusters on the nearby universe, under the supervision of Professor Ian Dell'Antonio. My job there consisted on searching the large telescopes public data archives for images of galaxy clusters and making galaxy catalogs to draw projected mass density maps based on the shape distortion of background galaxies created by those clusters.

The work is mainly divided into two parts, each of them versed in one of the two mentioned projects. Chapter 1 acts as a general introduction to some of the unsolved questions in Modern Cosmology, explaining the role the designed filter plays in the cleaning of CMB polarization signal to aid the detection of primordial gravitational waves, and providing a short theoretical background to the Weak Gravitational Lensing effect that allows the measurement of mass distribution in galaxy clusters. From there, the two projects are developed separately. In section 2.1, the reader will find the analytical expression for the point-like source profile in E- and B-modes, while in section 2.2, it will be proved that this very same profile satisfies the conditions to be a steerable wavelet. The properties and limitations of the designed filter will be further discussed in sections 2.2 and 2.3. The testing of filter performance on simulations of different regions of the microwave sky is left to section 2.5. Sections 3.1 and 3.2 respectively contain the description of the images and procedures used during my stay at Brown to map mass distribution in galaxy clusters. In particular, the results obtained for the Abell A2142 galaxy cluster are shown in section 3.3.

Index

CHAPTER 1

Unsolved questions in Modern Cosmology

Since Albert Einstein's General Relativity gave us the formalism to describe the evolution of space-time, and Edwin Hubble's observations of the cosmological redshift confirmed its expansion and pointed towards the idea of a young smaller hot universe, the *Cosmological Standard Model* has withstood many trials and tribulations. Reducing it to its bare essentials, the evolution of the universe as we understand it today is based on the Big-Bang concept and the Cosmological Principle of homogeneity and isotropy, establishing the humble absence of any privileged observer.

The story of the universe starts in an expanding infinitely dense singularity filled with a hot plasma of relativistic fundamental particles in thermal equilibrium. As space expands and wavelengths stretch out, the plasma progressively cools down. When temperature falls to $\sim$ 1GeV [3], the formation of bound states becomes energetically favorable against the quark-gluon state, creating the first baryons. By the first second, the universe is cold enough to favor the creation of the first light element nuclei. This period, known as *primordial nucleosinthesis*, lasts about three minutes and was thoroughly studied in the 1950s, producing very precise predictions of the relic abundances of light elements that should remain present today. As space keeps expanding, matter begins to dominate over radiation when temperature falls down to $\sim$1eV. At $\sim$0.1eV, the photons bathing space are no longer energetic enough to prevent the formation of neutral atoms. This new neutral matter, still in thermal equilibrium, becomes transparent to radiation and allows photons to roam freely for the first time in the history of the universe. The photons freed at that moment, known as the *recombination time*, are still present in the sky in an almost perfect blackbody spectrum, though redshifted to a much lower temperature of 2.725K. This radiation constitutes the *Cosmic Microwave Background* (CMB). From that moment on, gravity became the dominant force, attracting matter towards the small overdensities present at that time, and starting the bottom-up formation process that created the stars, galaxies and the filamentary large structure that we see nowadays.

The agreement between the light element abundances foretold in the primordial nucleosinthesis calculations and the ones measured today, the existence of the CMB, and the observation of the universe expansion, constitute the three observational pillars supporting the Cosmological Standard Model. However, the model just as presented before has some loose ends that scientists have been trying to tie down

for the last fifty years. Every measurement done in the era of precision cosmology agrees with a flat Euclidean universe of zero curvature. This flatness can only be achieved if the velocity distribution of the fluid filling the initial singularity has some very fine-tuned values. If velocities are slightly slower, the universe will quickly recollapse, and if they are slightly higher, the universe will expand too fast and doom itself to almost emptiness. An extremely smooth initial distribution of matter is also required to explain the tiny 10^{-5} inhomogeneities observed in the CMB [25]. Moreover, at the time of CMB's emission, approximately 380 000 years after the Big-Bang, only regions of the sky around one arc minute apart could have been causally connected, making really hard to explain how regions outside this causal horizon could have reached such level of homogeneity.

Therefore, the universe we know would only be possible assuming very specific initial conditions. These restrictions, known as the *flatness* and *horizon problems* respectively, make our universe a very lucky coincidence that doesn't sit very well with the general philosophy of the Cosmological Principle. In 1981, Alan Guth proposed the *inflationary universe* as a dynamical solution to both problems. Inflation consists of a period of exponentially accelerated expansion spanning $\sim 10^{-35}$s, when the scale factor grows around $\sim$21 orders of magnitude. This growing spurt stretched space so as to make any initial curvature almost flat, granting the compatibility of today's flatness with all kind of initial conditions. Before inflation, regions we see causally disconnected today were compressed to a much smaller space, allowing communication and a thermal equilibrium between them. After inflation, the sudden space expansion pulled these regions outside of each others causal horizons, freezing the homogeneous density distribution across the sky. Only with time, detached regions became causally connected again and started the process of gravitational collapse around the small overdensities present to form the structure we observe today. This inflation mechanism also explains why even though particle physics models predict the existence of magnetic monopoles, none have been found. Any monopole density produced before or during inflation would have been diluted enough to become undetectable after the accelerated expansion.

In the frame of General Relativity, inflation is caused by a negative pressure fluid, or equivalently, a constant energy density. The accelerated expansion is modeled as a slow-roll scalar potential, locating the universe in an initial high energy state that relaxes to a ground state via inflation. Several fields have been proposed, most of them creating *primordial gravitational waves* as the genuine observable product of the abrupt expansion, but a direct or indirect detection of these gravitational waves is still lacking.

In 1933, Fritz Zwicky was the first to point out another of the missing puzzle pieces of the Standar Cosmological Model, the existence of DM [16]. Studying the Coma Cluster, Zwicky found a big discrepancy between the mass he could infer using the total count of galaxies and the well-defined mass to luminosity ratios, and the gravitational mass he could obtain applying the virial theorem to the velocity dispersion of galaxies inside the cluster. Forty years later, Vera Rubin's galaxy rotation curves showed that luminosity and mass distribution didn't agree at the galactic scale either. Analyzing the orbits of stars around the galaxy with the same classical Newtonian model that applies to the Solar System, the galaxy luminosity distribution would suggest a steep increase on velocities around the bulge and a slow fall towards outer regions as less mass enters the inner radius. Instead, the curves show a plateau indicating that more mass keeps been added at the outer regions.

Some theories known as Modified Newtonian Dynamics (MONDs) explain this behavior by adding new terms only effective at cosmologically long distances to Newton gravitation. Although this approach may prove successful at the galaxy scale, other observational evidence outweights the balance towards the existence of an unknown only gravitational interacting kind of matter. The CMB measurements made by the Planck satellite result in a total matter density of $\Omega_m = 0.3089 \pm 0.0062$, corresponding only less than a fifth of that to ordinary baryon matter, $\Omega_b = 0.04860 \pm 0.00051$ [22]. The remaining percentage cannot be accounted for in terms of compact objects made of ordinary matter, such as brown dwarfs, neutron stars, unassociated planets or black holes, neither by weakly interacting almost massless neutrinos. Lots of *weakly interacting massive particles* (WIMPs), proposed mostly in supersymmetry models, are being considered to make the bulk of the dark matter present in the universe, although direct detections seem far away from now and characterization of DM properties through astrophysical measurements is the current way to rule out one candidate over the other.

The last addition to the Standard Cosmological Model was made in 1998, when two competing teams tried to measure the rate at which the universe expansion was slowing down due to the gravitational pull between matter. They repeated the diagram Hubble made back in the 1920s, but extending it to much larger distances using supernovae Ia as standard candles, and discovered that the universe expansion was actually accelerating. As with the accelerated expansion during inflation, this feature can be explained by a negative pressure fluid of constant energy. This energy would have been present through the whole history of the universe, but only recently became relevant when matter density diluted with expansion. The cosmological constant Λ, initially introduced by Einstein in his field equations to produce a static universe but later rejected when the universe was proved to be otherwise, reproduces this behavior. Apart from of its value, $\Omega_\Lambda = 0.6911 \pm 0.0062$ [22], little else is known about this fluid usually referred to as *Dark Energy*. Some efforts have been made to explain Dark Energy as the stress-energy of the vacuum, having contributions from the ground states of all quantum fields, but this leads to an estimated energy density of 120 orders of magnitude larger than the measured value [15]. This discrepancy is slightly alleviated in supersymmetric models, where the energy density is only 60 orders of magnitude larger than the measured value.

These three additions, cosmic inflation, Dark Matter and Dark Energy, complete the *Standard Cosmological Model*, also known as the ΛCDM model. The next sections are centered on the difficulties haunting the search for evidence of cosmic inflation in the CMB polarization, and in the use of Weak Gravitational lensing techniques to map DM distribution on galaxy clusters in an effort to characterize its interaction with ordinary matter and itself.

1.1 Observational evidence for Cosmic Inflation in Cosmic Microwave Background

1.1.1 Theory of Cosmic Microwave Background polarization

CMB light comes from the *recombination time*, a period when the universe cooled enough to start forming neutral hydrogen atoms, freeing photons from the particle plasma for the first time. These photons

interacted with not yet bound free electrons via Thomson scattering. As sketched in figure 1.1, Thomson scattering produces linearly polarized light in all but the incoming polarization direction. In a purely isotropic photon bath, with equal intensity photons incoming from every direction, Thomson scattering with free electrons will produce unpolarized light. Only when the incoming intensity in one direction surpasses the rest, the scattered radiation will be polarized. In particular, CMB polarization is the result of quadrupolar temperature anisotropies [25]. With a quadrupolar temperature pattern around a scatterer electron, hot along the y axis and cold in the x axis, linearly polarized light in the cold axis direction will be produced. The temperature inhomogeneities seen in CMB intensity maps implies this scenario of anisotropic incoming radiation, thus ensuring the polarization of the CMB signal.

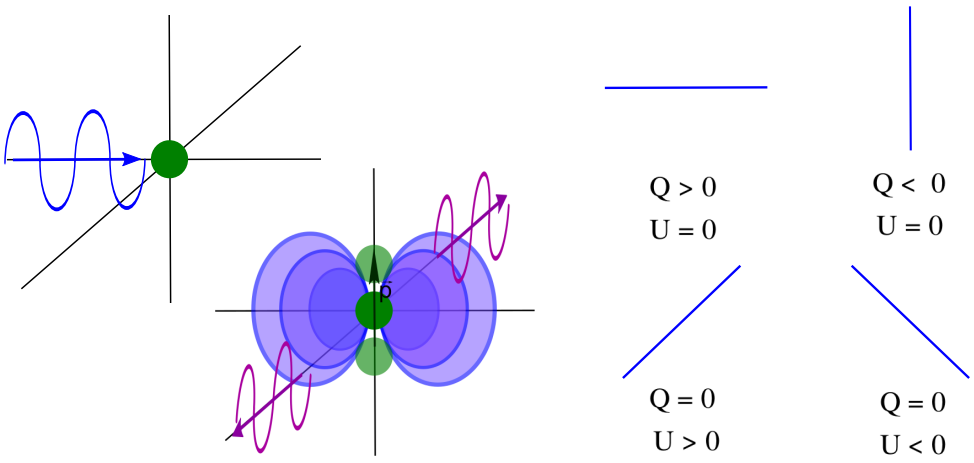

Figure 1.1: Left panel: When a photon excites a free electron, creating a dipole $\vec{p}$, the produced dipolar radiation emits linearly polarized light in all directions but the one of the incoming photon polarization. Right panel: Any linearly polarized ligth can be described with a combination of the Q and U Stokes parameters.

To retrieve the information encoded in CMB polarization, a formal characterization of its properties must be made [6]. The electric field vector of a generic monochromatic electromagnetic wave propagating along the $\vec{z}$ direction can be written in terms of its components as:

$$E_x = a_x \cos(\omega t - \zeta_x), \qquad E_y = a_y \sin(\omega t - \zeta_y), \tag{1.1}$$

and its polarization state can be described with the I, Q, U and V *Stokes' parameters*:

$$\begin{aligned} I &= a_x^2 + a_y^2, \\ Q &= a_x^2 - a_y^2, \\ U &= 2a_x a_y \cos(\zeta_x - \zeta_y), \\ V &= 2a_x a_y \sin(\zeta_x - \zeta_y). \end{aligned} \tag{1.2}$$

The I parameter is simply the intensity, Q quantifies the polarization along the $x-y$ direction, and U assesses the polarization along a 45° rotation of these axes. Therefore, a combination of Q and U can describe any linearly polarized light. The V parameter describes circularly polarized light, and since Thomson scattering only produces linearly polarized light, it is null for CMB photons. A rotation of the $x-y$ axes by an angle α implies a 2α rotation of the (Q, U) parameters, making them the components of

a spin-2 field. Limiting ourselves to a flat region of the sky, which is the common approach for the detection of point-like sources, this polarization field can be written as a symmetric trace-free 2x2 tensor like:

$$P_{ab} = \frac{1}{2}\begin{pmatrix} Q(\vec{r}) & U(\vec{r}) \\ U(\vec{r}) & -Q(\vec{r}) \end{pmatrix}, \tag{1.3}$$

where $Q(\vec{r})$ and $U(\vec{r})$ measure polarization in every point of the flat region. To extend this definition to the whole sky, the geometry of the sphere should be taken into account. Polarization can also be written as a complex number $Pe^{2i\phi}$ where $P = (Q^2 + U^2)^{1/2}$ is the *polarization intensity* and $\phi = \frac{1}{2}\arctan(U/Q)$ is the *polarization angle*, which measures its orientation relatively to the x axis. $Q(\vec{r})$ and $U(\vec{r})$ are locally defined at position $\vec{r}$, and therefore present the problem of being dependent on the selected coordinate system. To reach a polarization description independent of the coordinate system election, the polarization field can also be expressed in terms of the gradient and curl components of the tensor field, often called E- and B-modes in an analogy with the electromagnetic field:

$$\nabla^2 P_E = \partial_a \partial_b P_{ab}, \qquad \nabla^2 P_B = \epsilon_{ac}\partial_b \partial_c P_{ab}, \tag{1.4}$$

where ϵ_{ab} is the antisymmetric tensor. The explicit expressions in cartesian coordinates $\vec{q} = (q_x, q_y)$ of these P_E and P_B components in Fourier space read:

$$\begin{aligned} \tilde{P}_E(\vec{q}) &= \frac{1}{2}\frac{(q_x^2 - q_y^2)\tilde{Q}(\vec{q}) + 2q_x q_y \tilde{U}(\vec{q})}{q_x^2 + q_y^2}, \\ \tilde{P}_B(\vec{q}) &= \frac{1}{2}\frac{2q_x q_y \tilde{Q}(\vec{q}) - (q_x^2 - q_y^2)\tilde{U}(\vec{q})}{q_x^2 + q_y^2}, \end{aligned} \tag{1.5}$$

which can be written in polar coordinates $\vec{q} = (q, \theta)$ as:

$$\begin{aligned} \tilde{P}_E(\vec{q}) &= \frac{1}{2}[\cos 2\theta \tilde{Q}(\vec{q}) + \sin 2\theta \tilde{U}(\vec{q})], \\ \tilde{P}_B(\vec{q}) &= \frac{1}{2}[\sin 2\theta \tilde{Q}(\vec{q}) - \cos 2\theta \tilde{U}(\vec{q})]. \end{aligned} \tag{1.6}$$

1.1.2 Trails of Cosmic Inflation in Cosmic Microwave Background angular power spectra

The CMB temperature field $\Theta(\vec{n})$, defined as the normalized deviation (in the $\vec{n}$ direction on the sphere) from the average CMB temperature, $\Theta(\vec{n}) = \Delta T(\vec{n})/\bar{T}$, is usually decomposed in multipole moments $\theta_{\ell m}$

$$\Theta(\vec{n}) = \sum_{\ell=0}^{\infty}\sum_{m=-\ell}^{\ell} \theta_{\ell m} Y_{\ell m}(\vec{n}), \qquad \theta_{\ell m} = \int_\Omega \Theta(\vec{n}) Y^*_{\ell m}(\vec{n}) d\Omega, \tag{1.7}$$

where $Y_{\ell m}$ represent the spherical harmonics. The order m in the multipolar decomposition describes the angular orientation of fluctuations, and the order ℓ their angular size [3]. Since in the usual cosmic inflationary scenario the CMB radiation arises from random Gaussian fluctuations, the temperature field is fully characterized by its power spectrum, or equivalently, by its two-point correlation function. In addition, as the universe presents no privileged direction, CMB power spectrum is independent of m. Its angular power spectrum C_ℓ^{TT} is then defined as the variance of multipoles moments $< \theta^*_{\ell m}\theta_{\ell' m'} >= \delta_{\ell\ell'}\delta_{mm'}C_\ell^{TT}$, where the average is done over realizations with the same cosmology. For each angular scale ℓ, the best estimate of C_ℓ^{TT} is the average over all the $(2\ell + 1)$ m moments:

$$C_\ell^{TT} = \frac{1}{2\ell+1}\sum_{m=-\ell}^{l}|\theta_{\ell m}|^2. \tag{1.8}$$

The finite $(2\ell+1)$ number of m moments used to determine each C_ℓ^{TT} power limits the precision of its determination like:

$$\frac{\Delta C_\ell^{TT}}{C_\ell^{TT}} = \sqrt{\frac{2}{2\ell+1}}. \tag{1.9}$$

This feature, known as *cosmic variance*, severely affects the large scales, characterized by low ℓ multipoles, being much less dramatic for the small scales.

The multipole decomposition of CMB polarization field is a bit more complicated since the measured $Q(\vec{n})$ and $U(\vec{n})$ magnitudes describe a spin-2 field. This time, *second order spin-weighted spherical harmonics* $Y_{\ell m}^{\pm 2}$ must be used instead of classical spherical harmonics:

$$(Q \pm iU)(\vec{n}) = \sum_{\ell=2}^{\infty}\sum_{m=-\ell}^{\ell} a_{\ell m}^{\pm 2} Y_{\ell m}^{\pm 2}, \qquad a_{\ell m}^{\pm 2} = \int_\Omega (Q \pm iU)(\vec{n}) Y_{\ell m}^{*}(\vec{n})^{\pm 2} d\Omega. \tag{1.10}$$

Multipole moments $e_{\ell m}$ and $b_{\ell m}$ for E- and B-modes can then be computed from the multipole moments of the $(Q \pm iU)(\vec{n})$ field as:

$$e_{\ell m} = -\frac{1}{2}(a_{\ell m}^{+2} + a_{\ell m}^{-2}), \qquad b_{\ell m} = -\frac{1}{2i}(a_{\ell m}^{+2} - a_{\ell m}^{-2}), \tag{1.11}$$

making possible the calculation of the angular power spectra of E- and B-modes and the cross-correlation of them with the temperature field:

$$C_\ell^{EE} = \frac{1}{2\ell+1}\sum_{m=-\ell}^{\ell}|e_{\ell m}|^2, \qquad C_\ell^{BB} = \frac{1}{2\ell+1}\sum_{m=-\ell}^{l}|b_{\ell m}|^2, \qquad C_\ell^{TE} = \frac{1}{2\ell+1}\sum_{m=-\ell}^{\ell}\theta_{\ell m} e_{\ell m}^{*}. \tag{1.12}$$

Notice that, since, E-modes and T fields both behave as scalars under parity transformations, and B-modes act as pseudo-scalar fields, then, in the absence of parity violation physics, there is no correlation between E- and B-modes, $C_\ell^{EB} = 0$, and T and B-modes, $C_\ell^{TB} = 0$ [20]. Another consequence of this point is that tensor-like perturbations create both E- and B-modes, while scalar perturbations create only E-modes. Finaly, vector-like perturbations, although theoretically produce mainly B-modes, decay with the expansion of the universe and are not created as product of inflation.

CMB angular power spectra are extremely sensitive to most of the basic cosmological parameters, such as those defining its dynamics (like the current rate of expansion of the universe H_0, its curvature Ω_k and its matter Ω_m, baryon Ω_b and Dark Energy densities Ω_Λ) or the ones related to the initial energy density perturbations from inflation [25]. Different physical phenomena acting throughout the history of the universe also leave their mark on the spectra. C_ℓ^{TT}, C_ℓ^{EE} and C_ℓ^{BB} spectra, based on our current understanding of the universe, are shown in figure 1.2. The first peak in the temperature C_ℓ^{TT} spectrum, at $\ell \approx 200$, marks the horizon scale at the time of decoupling. The oscillations seen at smaller scales, $\ell > 200$, are the so called *Baryon Acoustic Oscillations* (BAO). This oscillations reflect how, before photon decoupling, the photon-baryon fluid was compressed as it fell into the gravitational wells of the small overdensities present at the moment, until the increase in the fluid's pressure forced it to expand

outward. The decrease in the fluid's pressure caused by its expansion, allows gravitational attraction to pull it back again, repeating the cycle. For progressively smaller scales, there is time for several compressions and rarefactions. This way, the maxima in the BAO present in temperature C_ℓ^{TT} spectrum reflect extrema in the photon-baryon fluid density. BAO also leave their imprint in the C_ℓ^{EE} spectrum, with a 90° offset with the C_ℓ^{TT} oscillations. To be generated, polarization needs for protons and electrons to not be so tightly coupled, therefore presenting its maxima in a 90° offset with respect to the fluid density, coupled instead with its velocity distribution [6]. The bulge in C_ℓ^{EE} and C_ℓ^{BB} spectra at low scales, $\ell < 10$, is the signature of the reionization the universe experienced at later times, creating a new source of polarization as Thomson scattering with free electrons was possible again.

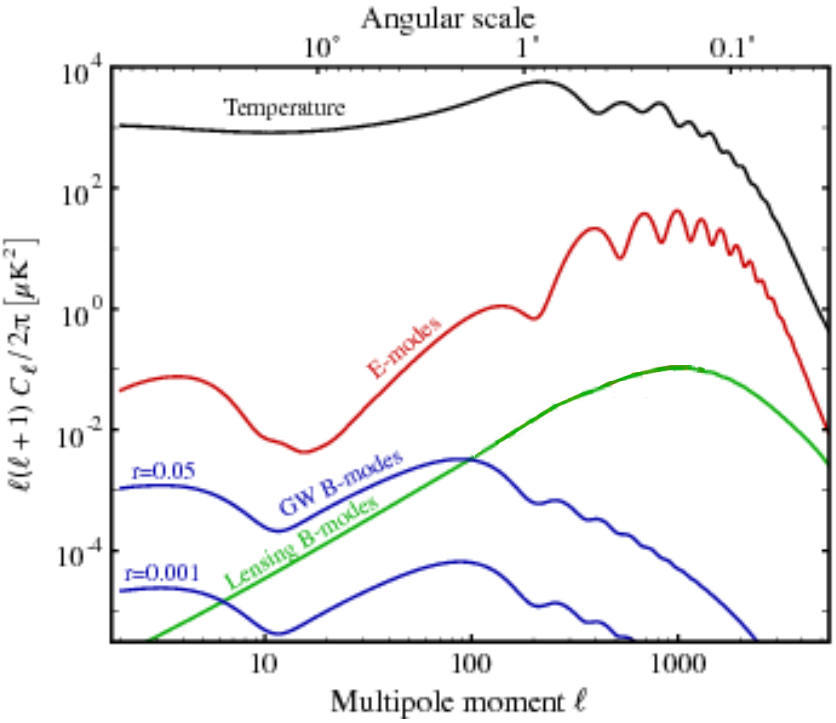

Figure 1.2: Theoretical predictions for the temperature (black), E-mode (red) and tensor B-mode (blue) power spectra. Primordial B-mode spectra are shown for values of tensor-to-scalar ratios $r = 0.05$ and $r = 0.001$. The expected values for the contribution to B-modes form gravitationally lensed E-modes (green) is also included. Image adapted from [9].

As previously mentioned, CMB power spectra is also an excellent probe for the initial density perturbations that acted as seeds for the formation of the structure seen today and for the primordial gravity waves generated by cosmic inflation. As scalar perturbations, density fluctuations affect temperature C_ℓ^{TT} and E-modes C_ℓ^{EE} spectra but no B-modes C_ℓ^{BB} spectrum, whereas primordial gravity waves, being tensorial perturbations of the metric, leave their mark across all power spectra. Usually, the amplitude of tensorial perturbations is defined normalized over the amplitude of scalar perturbations in what is known as the *tensor-to-scalar* ratio r. The tensor-to-scalar ratio plays a key role in the determination of a handful of the properties of the scalar field causing cosmic inflation. In particular, it is a direct measurement on the energy scale of inflation [3]

$$V_{\text{inflation}}^{1/4} \sim \left(\frac{r}{0.01}\right)^{1/4} 10^{16}\text{GeV}. \tag{1.13}$$

B-mode C_ℓ^{BB} power spectrum turns out to be very sensitive to the value of the tensor-to-scalar ratio, as can be seen in figure 1.2. This feature, combined with the fact that only tensorial perturbations produce

B-modes, makes the B-mode angular power spectrum the smoking gun for primordial gravitational waves indirect detection.

The main problem slowing this course of action is the accuracy with which the faint CMB polarization signal must be measured, especially at large scales, in order to allow a good determination of r. CMB polarization signal is obscured by several foregrounds through its whole frequency spectrum, making imperative the development of component separation techniques. In addition, gravitational lensing alters the E and B nature of polarization patterns as the light passes through the large-scale structure present in the late universe. As a result, power is transferred from the E- to the B-mode, creating a scalar component that should not be present in the otherwise tensorial-only B-mode signal. This phenomenon affects mostly the small scales, completely obscuring the B-mode tensorial power spectra that would be created by tensor-to-scalar ratios of $r < 10^{-3}$. The best measurement of the tensor-to-scalar ratio determined to date by the Planck satellite sets an upper limit to its value of $r < 0.09$ [22].

1.1.3 Foregrounds obscuring intensity and polarization Cosmic Microwave Background signal

Several physical processes within our galaxy result in the emission of light in the CMB's frequency range, presenting a stronger signal than that of the CMB throughout most of the spectrum, as can be seen in figure 1.3. Since this light emissions take place way after CMB emission, they are often called *foregrounds* rather than backgrounds. Dismissing atmospherical emissions, foregrounds in the CMB's frequency range come from synchrotron, free-free, thermal dust and spinning dust radiation. A general description of the properties of these galactic foregrounds is given in [11].

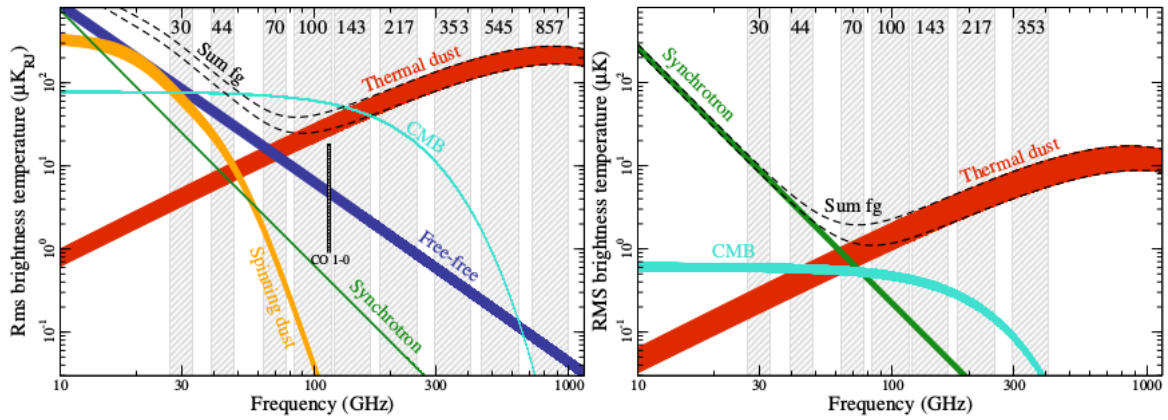

Figure 1.3: Foregrounds obscuring CMB intensity (left) and polarization (right) signal through all frequency Planck channels. Image taken from [22].

Synchrotron radiation occurs when relativistic cosmic rays and electrons are accelerated by the galatic magnetic field, spiraling around the field lines and emitting radiation. Synchrotron spectrum is well approximated by a power-law for a great range of frequencies, and depends mostly on the number and energy spectrum of electrons and the strength of the magnetic field. Synchrotron emission produces

polarized light, reaching a polarization fraction up to 75% in the presence of uniform and regular magnetic fields. However, line-of-sight depolarization and the irregular galactic magnetic field reduce the polarization fraction to around 10-40%, which is still above the typical polarization level of CMB emission.

Free-free radiation, or thermal bremsstrahlung, is produced when free electrons within ionized clouds of gas are accelerated by ions. These interactions produce unpolarized light since they present random orientations. A residual polarization fraction can be generated at cloud edges, where privileged directions do exits, being the measured upper limit of $< 3\%$.

Interstellar dust grains heated to around $T \approx 20$K emit what is known as *thermal dust* radiation. This emission is modeled as a *gray body*, a blackbody spectrum modified by opacity effects and by the different emissivity dust grains present for each wavelength. Thermal dust emission can be significantly polarized, since elongated dust grains emit preferentially along their shortest axes and large dust grains efficiently align themselves with the galactic magnetic field, being possible for its polarization fraction to reach values varying from 5 to 20% in different regions of the sky. These interstellar dust grains also rotate, emitting dipolar radiation when they present an eletric dipole moment. This mechanisim of emission is often referred to as *spinning dust* radiation. The smallest grains, of around $\sim$1nm, can rotate at CMB frequencies due to their lower moments of inertia, dominating the spinning dust emission. Theoretical arguments suggest that spinning dust radiation has a low polarization fraction for CMB frequencies, while observations set the upper limits at a few percent. Spinning dust radiation is the main candidate to explain the *anomalous microwave emission* (AME), an excess emission in the 10-60 GHz frequency range that can not be justified by thermal dust, synchrotron or free-free mechanisms.

Despite the aforementioned effects of foregrounds, CMB intensity signal still dominates between $\sim$ 40-100 GHz, allowing for an observation window. However, while only two of the four galactic foreground sources produce a significant amount of polarized light, foregrounds still dominate over CMB polarization emission due to their greater polarization fractions and their similar emissivity in E- and B-modes. In addition to these diffuse foregrounds, galaxies outside of our own present the same emissions, constituting compact sources of polarized light. Known generically as *extragalactic point-like sources*, as they are far enough to not be spatially resolved by CMB detectors, they act as another foreground affecting small scales. Although nowadays extragalactic point-like sources are thought to have small polarization fractions and their effects are easily mitigated by detecting them in intensity maps and masking them, they possess the possibility of becoming a major problem in the future, when de-lensing techniques clear the small scales of the gravitational lensing transferred B-modes. This prospective, along with the little attention they currently draw in the bibliography, motivates the focus of this work on these extragalactic point-like sources. Though the first objective is still their removal from CMB polarization signal, their detection and characterization also apports useful information to extragalactic astrophysicists.

1.2 Characterization of Dark Matter nature via astrophysical observations

1.2.1 Review of the current understanding of Dark Matter

As previously discussed, DM is a fundamental component of the *Standard Cosmological Model*. Its presence alters the paradigm of structure formation, as compared to a scenario driven only by gravitationally bound baryonic matter, adding a new component that leaves its marks in different cosmological and astrophysical observables. DM properties are also trying to be determined in particle colliders and direct detection experiments, although so far, the majority of the constraints set to its nature come from cosmological and astrophysical indirect detections and observations.

To be consistent with astronomical observations, DM candidates must reproduce the abundances measured in galactic halos and galaxy clusters, as well as the overall relic density obtained from the CMB angular power spectra. They must also be stable at cosmological time scales because, otherwise, they would have decayed by now. DM candidates should honor their name and not interact with electromagnetic radiation, leaving gravitational attraction as apparently the only interaction allowed between dark and ordinary matter. DM's neutrality, apart from being the reason why DM is hidden from our telescopes, is required to produce the large-scale structure we observe today. The small anisotropies measured in the CMB impination were not large enough to justify the formation of today's large-scale structly that the fluctuations in ordinary matter density present at the time of recombure [16]. With only the measured fluctuations in ordinary matter density as seeds, the structure we see today would not have time to form. Therefore, DM must be electrically neutral in order to start its collapsing process way before the recombination time, and broaden the potential wells in which ordinary matter will start to fall once it becomes neutral.

The comparison between the large-scale structure observed in sky surveys and the results obtained from N-body simulations (emulating the gravitational collapse of baryonic and dark matter to slowly forms structure), are also being used to further constrain the properties of DM. These simulations reaffirm the idea that DM presence is necessary to form the filamentary-like large structure we see today. However, when simulations are run with relativistic DM, also referred to as *hot* DM, structure formation is retarded or even wiped out. Therefore, DM particles must be non-relativistic, or *cold*.

The DM candidates fulfilling the aforementioned conditions that are being considered today are primordial black holes, axions, sterile neutrinos and all sort of *weakly interacting massive particles* or WIMPS [12]. Some cosmological models predict that a *primordial* type of black holes could have been formed in the very early stages of the universe, when the high densities and inhomogeneous conditions may have created sufficiently dense regions to undergo gravitational collapse [8]. They are hypothesized to have a very wide range of masses and to slowly evaporate away due to Hawking radiation. Axions are light particles that were proposed by Peccei and Quinn to explain why CP-symmetry doesn't seem to be broken in QCD. Peccei and Quinn postulated that a new symmetry prevents the appearance of the electric dipole moment the Lagrangian of the strong force grants to neutrons in the same way that gauge symmetry makes photons massless [21]. They also theorized that this new symmetry could be slightly broken, creating a new light scalar particle, the axion. Although axions are thought to be extremely light,

some theories give them masses of $\sim \mu$eV, if they exist in large enough numbers, they can still be the major component of cold DM. The discovery of the non-zero mass of neutrinos suggested the existence of some new SU(3)×SU(2)×U(1) singlet fermions, a form of right-handed neutrinos [5]. These new particles, known since then as *sterile neutrinos*, are supposed to only interact gravitationally and to decay into the usual *active* neutrinos emitting photons in the X-ray range. Apart from being a candidate for warm DM, sterile neutrinos would also play a role in pulsar kicks, star formation and the physics of supernovae. Some of the most popular WIMP candidates for DM come from supersymmetry (SUSY) models. SUSY counts with an additional symmetry that allows the conversion of fermions into bosons and vice-versa. This way, every fermion in the Standard Model would have a superpartner boson, and every boson, a superpartner fermion, doubling up the total number of particles. Amongst all these new particles, *neutralinos*, a superposition of the neutral superpartners of the Higgs and gauge bosons, stand out as the best candidates for DM [24]. Neutralinos are electrically neutral and weakly interacting and are predicted to have a large mass. They would be stable since a symmetry known as R-parity would prevent them from decaying into lighter particles the same way the conservation of baryonic number prevents protons from decaying. Therefore, their relic abundance could be of cosmological significance.

1.2.2 Exploring Dark Matter self-interactions through its distribution in Galaxy Clusters

Mergers of galaxy clusters turn out to be an excellent laboratory to study interactions between baryonic and dark matter. The most famous one, the *Bullet Cluster*, is considered by some to be the smoking gun proof of DM existence [16]. Galaxy clusters are essentially composed of galaxies, hot intracluster gas and DM. The galaxies forming the clusters can typically stand Megaparsecs away from each other, so in the Bullet Cluster, when a sub-cluster collided into the larger galaxy cluster 1E 0657-56, the galaxies within both clusters just passed through each other without interacting. However, the intracluster gas got compressed and shock heated, emitting a great amount of X-ray radiation that can be used to trace the position of the gas. As the intracluster gas concentrates the majority of the baryonic mass of galaxy clusters, this X-ray emission effectively locates where the baryonic matter is after the collision. Using now Weak Gravitational Lensing techniques, we can also map the total distribution of mass in the cluster. Overlaying these two results reveals that although the intracluster gas got decelerated in the collision and lagged behind, both the galaxies and the majority of the mass continued forward. This result proved at the same time the existence of DM, since the observed behaviour would be extremely difficult to explain within MOND theories, and the colisionless nature of DM.

Some DM models argue that, although DM interaction with ordinary matter is clearly extremely weak, there is no reason why DM could not significantly interact with itself [29]. This train of thought opens up a new *dark sector* of gauges forces beyond the Standard Model to describe DM self-interactions. Aside from this tantalizing glimpse at new physics, evidence of DM self-interactions will also help to further constrain the usual DM candidates. Mergers of galaxy clusters are again the best laboratory to test this *Self-Interacting Dark Matter* (SIDM) models, since they allow us to trace the movement of a DM halo through a high DM density background.

Figure 1.4: Optical image of the Bullet Cluster where X-ray emission has been overlaid in pink and the mass distribution obtained from Weak Lensing maps is shown in blue. Credits:X-ray, NASA/CXC/CfA/M.Markevitch et al.; optical, NASA/STScI and Magellan/U.Arizona/D.Clowe et al.; lensing map, NASA/STScI, ESO WFI and Magellan/U.Arizona/D.Clowe et al.

In the scenario previously discussed for the Bullet Cluster, the gravitational lensing map showed that the majority of the mass in both clusters passed relatively undisturbed through each other. Just from this observations, limits on the value of the cross-section of DM self-interaction could be set. However, as discussed in [19], more interesting results can be draw from the DM and galaxies distribution after the collision. If DM was indeed interacting with itself, it would experience the same drag force with fluid-like properties that deccelerated the intracluster gas. This way, the DM distribution after the collision should slightly deviate from the galaxy distribution. DM self-interactions force some galaxies and DM particles to escape their combined gravitational potential and to move in highly elliptical orbits, inducing an asymmetry in the respective galaxies and DM distributions. This perturbation maintains coupled the peaks of galaxies and DM distributions, but separates their centroids. Due to the very distinct shapes they induce in the final galaxies and DM distributions, two kinds of self-interactions must be considered: frequent collisions with small momentum transfer and rare collisions with great momentum transfer. If self-interactions are frequent and present a small momentum transfer, all DM particles will suffer a large number of collisions and effectively be deccelerated. While the DM halo slows it progress as a whole, some of the loosely bound galaxies will escape the system and continue forward, leaving the galaxies distribution with a tail in the forward direction whereas the DM distribution will maintain its shape. On the other hand, if DM self-interactions are rare but possess large momentum transfer, only a small number of DM particles will scatter. The large momentum transfer ensures that the few DM particles that do scatter, either get ejected from the system in the direction opposite to the direction of motion, or get pushed into highly elliptical orbits. Thus this time, it will be the DM distribution the one that develops a tail in the backward direction while the galaxies distribution will remain unaltered.

In such manner, a precise determination of the galaxies and DM distribution will allow us to differentiate between these two kinds of interactions. For said precision on the determination DM distrution to be possible, high resolution Weak Gravitational Lensing maps of the clusters are needed. The basics behind the Weak Gravitational effect used to map the DM distribution and its hardships and limitations will be

contemplated in the following section.

1.2.3 Weak Lensing limit

One of the many successful predictions of General Relativity is the gravitational lensing effect. Photons move along trajectories of minimum action, which in a flat space correspond to straight lines, but in the curved space-time framework of General Relativity, get generalized to geodesics. Therefore, a large mass in the line-of-sight of an observer will significantly curve the space-time around it producing curved geodesics for photons to follow. Extending back the trajectories of the received photons as straight rays, the observer will see the original source as if through a traditional lens, suffering the same magnifying and distorting effects.

In this disposition of source, disturbing mass and observer, it is useful to describe the lens through the *inverse magnification matrix*

$$M^{-1} = (1-\kappa)\begin{pmatrix} 1 & 0 \\ 0 & 1 \end{pmatrix} + \gamma \begin{pmatrix} \cos 2\phi & \sin 2\phi \\ \sin 2\phi & -\cos 2\phi \end{pmatrix}, \tag{1.14}$$

which describes how the original shape and size of the source are altered under a change in the shape and size of its image through the lens[1]. The *convergence*, (κ), and *shear*, (γ), terms are related to the physical properties of the lens, as linear combinations of the second derivatives of the deflection angle. The convergence term produces an isotropic magnification, and can be interpreted as the projected mass density over the critical density. Shear, on the other hand, represents the distorting effect of the lens, quantifying the stretching in the ϕ direction. It is a non-local magnitude, depending its value (at any given point on the sky) on the mass distribution everywhere, consequently not having such a straightforward interpretation as κ.

Gravitational lensing has a very obvious effect in the *Strong Lensing* regime, where objects are perfectly aligned behind massive galaxies or galaxy clusters, producing colorful arcs and multiple images. However, to study the mass distribution of regions away from this very dense points, small shape distortions over a large number of sources must be statistically studied. This is the domain of *Weak Lensing* (WL). As it is explained in the general description of WL techniques made in [31], galaxy shapes are approximated as ellipses, thus being characterized by their ellipticity components e_+ and $e_\times$:

$$\begin{aligned} e_+ &= \frac{I_{xx} - I_{yy}}{I_{xx} + I_{yy}}, \\ e_\times &= \frac{2I_{xy}}{I_{xx} + I_{yy}}. \end{aligned} \tag{1.15}$$

This ellipticity components are computed through the quadrupole moments I_{xx}, I_{yy} and $I_{x,y}$, which in turn can be calculated from the intensity distribution $I(x, y)$ in optical images as:

[1] A complete and rigorous deduction of this matrix and the whole gravitational lensing formalism can be found in [10].

$$I_{xx} = \frac{\sum I(x,y)\omega(x,y)x^2}{\sum I(x,y)\omega(x,y)},$$
$$I_{yy} = \frac{\sum I(x,y)\omega(x,y)y^2}{\sum I(x,y)\omega(x,y)},$$
$$I_{xy} = \frac{\sum I(x,y)\omega(x,y)xy}{\sum I(x,y)\omega(x,y)}, \tag{1.16}$$

where x and y coordinates describe the position of every point in the image and the sum is done over all the contiguous pixels identified as a part of a galaxy. The weighting function $\omega(x,y)$, usually a circular or elliptical Gaussian, is introduced to deweight the outer pixels with low S/N ratio.

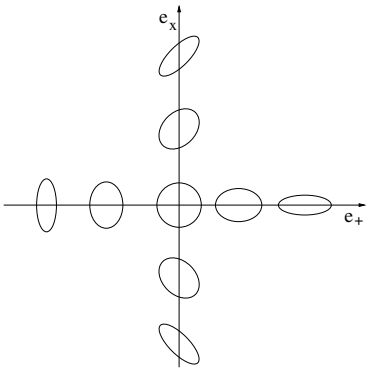

Figure 1.5: Shape of the ellipses described by different values of the e_+ and $e_\times$ ellipticity components. The $+$ and $\times$ names are inspired by how each component influences the final shape of the ellipse. Image taken from [31].

Ellipticity components e_+ and $e_\times$ are related to the scalar ellipticity ϵ and position angle ϕ as

$$\epsilon = \sqrt{e_+^2 + e_\times^2} \qquad \phi = \frac{1}{2}\arctan\left(\frac{e_\times}{e_+}\right), \tag{1.17}$$

and can be written as a *complex ellipticity*, $e_i = \epsilon e^{i2\phi}$. In regions of the sky far away from any lensing mass, the observed e_i distribution is roughly Gaussian with zero mean. Hence, assuming that in the absence of any lens, galaxy shapes are randomly oriented, any departure from zero of the mean ellipticity can be attributed to a lensing effect. When the mean elliptity of source background galaxies is near this zero mean regime ($\langle\epsilon_S\rangle \approx 0$), the intrinsic and the lens induced ellipticities add up linearly, being the effect of the magnification matrix on the complex ellipticity, $\epsilon_I = \epsilon_S + \frac{2\gamma}{1-\kappa}$, where the subscripts stand for the source, S, and image, I, ellipticities. For this calculation, a constant magnification across the source is assumed. This assumption is valid for typical sources of few arc seconds of size, but obviously excludes very large sources or those near caustics. Averaging over many sources, since $\langle\epsilon_S\rangle = 0$ is assumed, we get:

$$\langle\epsilon_I\rangle = \left\langle\frac{2\gamma}{1-\kappa}\right\rangle. \tag{1.18}$$

In most cases, the projected mass density is so small that the $\kappa \ll 1$ approximation can be applied, ending with $\langle\epsilon_I\rangle \approx \langle 2\gamma\rangle$. This approximation of constant magnification and $\kappa \ll 1$ is known as the *Weak Lensing limit* and is applicable for the vast majority of the universe, being one of the most powerful direct probes to study mass distributions since it doesn't rely on other assumptions such as hydrostatic equilibrium or galaxy distribution proxies.

However, the Weak Lensing limit approximation also has its limitations. Its statistical nature makes necessary the use of a very large number of galaxies to achieve a good angular resolution and extra

information is needed about the distance between the lens and the observer, the observer and the source, or the lens and the source in order to pass from projected mass density to actual measurements of mass. Knowledge of shear alone does not allow for mass distribution measurements either, due to the problem known as *mass sheet degeneracy*. A uniform sheet of mass induces only magnification, and because of the linearity of the equations, any mass sheet could be added or subtracted without altering shear measurements. Any alignments or distortions on the shape of galaxies that displace their mean ellipticity from zero, which can be caused by a wide range of effects, from the anisotropies introduced in the shape of galaxies by the telescope's *point spread function* (PSF) to cosmic shear, also endanger the applicability of the fundamental $\langle \epsilon_S \rangle = 0$ assumption sustaining WL formalisms.

CHAPTER 2

Filter design

2.1 Point-like source profile in E- and B-mode maps

As with the rest of galactic foregrounds, extragalactic point-like sources emission is linearly polarized, thus being fully characterized by its polarization intensity P, polarization angle ϕ and position in the sky. In terms of the Q and U Stokes' parameters, an extragalactic source located at a $\vec{r_i}$ position will be described as

$$Q(\vec{r_i}) = \rho(\vec{r})P\cos 2\phi, \qquad U(\vec{r_i}) = \rho(\vec{r})P\sin 2\phi), \tag{2.1}$$

with $\phi \in [0, \pi)$ and $\rho(\vec{r}) = \delta(\vec{r} - \vec{r}_i)$. Assuming sources were already detected in intensity maps using the conventional detection mechanisms [23] and their positions are already known, the desired filter aims to obtain these P and ϕ parameters. As customary for the detection of compact sources, the filter will be applied to the projection onto the plane of a sky small square region containing the source. The smaller surface of work allows for a better statistical characterization of the background surrounding the source, improving filter performance. The small size and compact nature of point-like sources ensure that, when pixels in the plane and in the sphere have approximately the same size, no significant distortion in the shapes of point-like sources will be introduced by the projection.

Detectors used to measure CMB intensity and polarization maps usually have a Gaussian PSF, giving a Gaussian contour to the otherwise ideally point-like sources. Centering the coordinate origin at the point-like source, its Gaussian profile in polar coordinates $\vec{r} = (r, \xi)$ in the real plane is given by:

$$\rho(r) = \frac{1}{2\pi\sigma^2} e^{-r^2/2\sigma^2}, \tag{2.2}$$

being fully characterized by the FWHM of the PSF, or alternatively, its σ. The relationship between these two magnitudes is $\sigma = \mathrm{FWHM}/2\sqrt{2\ln 2} \approx \mathrm{FWHM}/2.355$. In Fourier space, this profile transforms as:

$$\tilde{\rho}(q) = \frac{\sigma^2}{2\pi} e^{-q^2\sigma^2/2}. \tag{2.3}$$

where $\vec{q} = (q, \theta)$ are the polar coordinates in the reciprocal space. Attending to equations (1.6), the source profile in Fourier space could be written in E- and B-mode maps as:

$$\begin{aligned} \tilde{P}_E(\vec{q}) &= \frac{P}{2}[\cos 2\theta \cos 2\phi + \sin 2\theta \sin 2\phi]\tilde{\rho}(q), \\ \tilde{P}_B(\vec{q}) &= \frac{P}{2}[\sin 2\theta \cos 2\phi - \cos 2\theta \sin 2\phi]\tilde{\rho}(q). \end{aligned} \tag{2.4}$$

This can be transformed to real space, providing a profile given by:

$$P_E(\vec{r}) = \frac{P}{4\pi^2}[\cos 2\xi \cos 2\phi + \sin 2\xi \sin 2\phi]\tau(r),$$
$$P_B(\vec{r}) = \frac{P}{4\pi^2}[\sin 2\xi \cos 2\phi - \cos 2\xi \sin 2\phi]\tau(r), \tag{2.5}$$

with

$$\tau(r) = \frac{\sigma^2}{r^2}\left[e^{-r^2/2\sigma^2}\left(1 + \frac{r^2}{2\sigma^2}\right) - 1\right]. \tag{2.6}$$

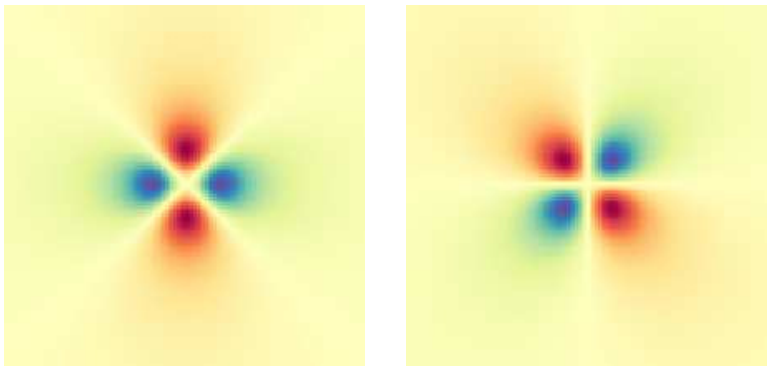

Figure 2.1: $P_E(\vec{r})$ and $P_B(\vec{r})$ point-like sources profiles in E- and B-modes, respectively, for a polarization angle of $\phi = 0$ and a FWHM of 20 pixels.

The complete mathematical deduction of equations (2.5) and (2.6) is done in Appendix A. As can be seen in figure 2.1, these equations produce a hot and cold two-lobes profile. The position of the hot and cold lobes is the opposite of what would be expected by just looking at the angular component of equations (2.5) because the radial component $\tau(r)$ has a negative amplitude. The symmetry between the sine and cosine terms in the equations, both for the polar ξ and polarization ϕ angles, introduces 45° rotation relationships between the E- and B-mode profiles. A 45° spatial rotation, fixing the polarization angle, transforms the E profile into the B one, $P_E(r, \xi \pm \pi/4, \phi) = \mp P_B(r, \xi, \phi)$. This property manifests itself in the plots shown in figure 2.1, and could be very useful in crossmatching mechanisms between E- and B-modes to verify detections. Another useful relationship is $P_E(r, \xi, \phi \pm \pi/4) = \pm P_B(r, \xi, \phi)$, i.e., the equality between E- and B-modes under a 45° rotation in the polarization angle. These angular symmetries make P_E and P_B *steerable functions*, i.e., functions that can be written as linear combinations of rotated versions of themselves [14]. Steerable functions are written in terms of the *interpolation functions* $k_j(\phi)$:

$$f^{\phi}(\vec{r}) = \sum_{j=1}^{M} k_j(\phi) f_j^{\phi}(\vec{r}). \tag{2.7}$$

It can be proved that both, P_E and P_B, verify the two conditions imposed to steerable functions: being expandable in a Fourier series in polar angle ϕ, and having interpolation functions solutions of the system:

$$\begin{pmatrix} 1 \\ e^{i\phi} \\ \dots \\ e^{iN\phi} \end{pmatrix} = \begin{pmatrix} 1 & 1 & \dots & 1 \\ e^{i\phi_1} & e^{i\phi_2} & \dots & e^{i\phi_M} \\ \vdots & \vdots & \vdots & \vdots \\ e^{iN\phi_1} & e^{iN\phi_2} & \dots & e^{iN\phi_M} \end{pmatrix} \begin{pmatrix} k_1(\phi) \\ k_2(\phi) \\ \dots \\ k_M(\phi) \end{pmatrix}. \tag{2.8}$$

Let us prove that the P_E profile verifies these conditions. In addition, in order to make the demonstration valid for both, Fourier and real spaces, we will express P_E in terms of some general polar coordinates $\vec{s} = (s, \alpha)$, and all radial dependences and constants will be absorbed into a $\eta(s)$ profile, maintaining only the notation of the polarization angle ϕ:

$$P_E(s, \alpha, \phi) = [\cos 2\alpha \cos 2\phi + \sin 2\alpha \sin 2\phi]\eta(s). \tag{2.9}$$

This expression is a generalization of the P_E given in equations 2.3 and 2.4. Hence, P_E can then be expanded in a Fourier series:

$$P_E(s, \alpha, \phi) = \sum_{n=-N}^{N} a_n(s, \alpha) e^{in\phi}, \tag{2.10}$$

with coefficients $a_n(s, \alpha)$ given by:

$$a_n(s, \alpha) = \frac{1}{2\pi} \int_{-\pi}^{\pi} P_E(s, \alpha, \phi) e^{-in\phi} d\phi. \tag{2.11}$$

As $P_E(s, \alpha, \phi)$ already has an angular ϕ dependency, it is immediate that the only non-zero coefficients will be those with $n = \pm 2$. The Fourier series expansion of P_E is then:

$$P_E(s, \alpha, \phi) = \frac{1}{2}\eta(s)\Big(e^{-2i\alpha} e^{2i\phi} + e^{2i\alpha} e^{-2i\phi}\Big). \tag{2.12}$$

In this case, just two interpolation functions suffice to fulfill the steering condition:

$$\Big(e^{2i\phi}\Big) = \Big(e^{2i\phi_1} \quad e^{2i\phi_2}\Big) \begin{pmatrix} k_1(\phi) \\ k_2(\phi) \end{pmatrix}. \tag{2.13}$$

Choosing $\phi_1 = 0$ and $\phi_2 = \pi/4$, the interpolation functions are simply $k_1(\phi) = \cos 2\phi$ and $k_2(\phi) = \sin 2\phi$. Therefore, P_E at any polarization angle can be expressed as:

$$P_E(s, \alpha, \phi) = \cos 2\phi P_E(s, \alpha, 0) + \sin 2\phi P_E(s, \alpha, \pi/4). \tag{2.14}$$

Using the $P_E(r, \xi, \phi \pm \pi/4) = \pm P_B(r, \xi, \phi)$ property, it is trivial to prove that P_B is also steerable:

$$P_B(s, \alpha, \phi) = \cos 2\phi P_B(s, \alpha, 0) + \sin 2\phi P_B(s, \alpha, \pi/4). \tag{2.15}$$

2.2 Filter definition

When designing the filter and, taking a look at P_E and P_B as written in equations (2.14) and (2.15), it seems very straightforward to use $P_E(s, \alpha, 0)$ and $P_E(s, \alpha, \pi/4)$ as filtering functions. Therefore, we define the following filtering functions

$$\psi_x(s, \alpha, R) = \cos 2\alpha \eta(s), \qquad \psi_y(s, \alpha, R) = \sin 2\alpha \eta(s), \tag{2.16}$$

where R is known as the *filter scale*, and generalizes the σ parameter previously introduced in the definition of the radial components of both, Fourier $\tilde{\rho}(q)$ and real space $\tau(r)$, source profiles. As happened before, $\psi_y(s, \alpha, R)$ is also the 45° rotation of $\psi_x(s, \alpha, R)$, $\psi_y(s, \alpha, R) = \mp\psi_x(s, \alpha \pm \pi/4, R)$, hence, we can define a *steerable wavelet* where ψ_x and ψ_y are respectively the $\alpha = 0$ and $\alpha = \pi/4$ rotations of the *mother wavelet*:

$$\Psi(s, \alpha, R) = \cos 2\alpha \eta(s, R). \tag{2.17}$$

We call it *wavelet*, not only due to the introduction of the scale, but also because $\Psi(s,\alpha,R)$ verifies the conditions required to be a wavelet in the plane [30] since it is a *compensated function*:

$$\int_0^\infty \int_0^{2\pi} \Psi(s,\alpha,R) s ds d\alpha = \int_0^\infty s\rho(s) ds \int_0^{2\pi} \cos 2\alpha d\alpha = 0. \tag{2.18}$$

Obviously, as a steerable wavelet, $\Psi(s,\alpha,R)$ makes possible the reconstruction of the P_E and P_B profiles through a linear combination of the images of the source filtered with the ψ_x and ψ_y basis functions. This way, any polarization angle can be reproduced by filtering only with two functions, allowing for a fast and powerful filtering process. The wavelet coefficients of the filtered images ω_x^E and ω_y^E are computed as

$$\begin{aligned}
\omega_x^E(r,\xi,\phi,R) = P_E(r,\xi,\phi) \otimes \psi_x(r,\xi,R) = IFT\Big[\tilde{P}_E(q,\theta,\phi)\cdot\tilde{\psi}_x(q,\theta,R)\Big] = \\
= IFT\Big[\frac{R^2}{2\pi}\cos 2\theta e^{-q^2R^2/2}\tilde{P}_E(q,\theta,\phi)\Big], \\
\omega_y^E(r,\xi,\phi,R) = P_E(r,\xi,\phi) \otimes \psi_y(r,\xi,R) = IFT\Big[\tilde{P}_E(q,\theta,\phi)\cdot\tilde{\psi}_y(q,\theta,R)\Big] = \\
= IFT\Big[\frac{R^2}{2\pi}\sin 2\theta e^{-q^2R^2/2}\tilde{P}_E(q,\theta,\phi)\Big],
\end{aligned} \tag{2.19}$$

where $IFT[x]$ stands for the inverse Fourier transform of the function x, and $\otimes$ denotes standard convolution. Wavelet coefficients ω_x^B and ω_y^B have an analogous definition. Since ψ_x and ψ_y have the same functional form than the $P_E(s,\alpha,0)$ and $P_E(s,\alpha,\pi/4)$, as happened in equations (2.14) and (2.15), the proper linear combination of the wavelet coefficients $\omega_x^{E,B}$ and $\omega_y^{E,B}$ can be written down to reconstruct the original E- and B-modes profiles:

$$\begin{aligned}
\omega_E(r,\xi,\phi,R) = \cos 2\phi\omega_x^E(r,\xi,\phi,R) + \sin 2\phi\omega_y^E(r,\xi,\phi,R), \\
\omega_B(r,\xi,\phi,R) = \cos 2\phi\omega_y^B(r,\xi,\phi,R) - \sin 2\phi\omega_x^B(r,\xi,\phi,R).
\end{aligned} \tag{2.20}$$

Therefore, it is clear that to define a method to estimate the value of the polarization angle, ϕ, becomes the crucial part of the filtering process.

A optimal way to find an estimation of the polarization angle ($\hat{\phi}$) can be defined by looking at the equations that describe ω_x^E and ω_y^E filtered images. Computing the inverse Fourier transforms previously presented in equations (2.19), the ω_x^E and ω_y^E wavelet coefficients have a real space profile given by:

$$\begin{aligned}
\omega_x^E(r,\xi,\phi,R) = \frac{P}{16\pi^2}\frac{\sigma^2R^2}{\sigma^2+R^2}\Big[\cos 2\phi e^{-z} + \Big(\cos 4\xi\cos 2\phi + \sin 4\xi\sin 2\phi\Big)\lambda(z,R)\Big], \\
\omega_y^E(r,\xi,\phi,R) = \frac{P}{16\pi^2}\frac{\sigma^2R^2}{\sigma^2+R^2}\Big[\sin 2\phi e^{-z} + \Big(\sin 4\xi\cos 2\phi - \cos 4\xi\sin 2\phi\Big)\lambda(z,R)\Big],
\end{aligned} \tag{2.21}$$

where the radial dependence $\lambda(z,R)$ reads:

$$\lambda(z,R) = \frac{1}{2\pi z^2}\Big[e^{-z}\Big(z(z+4)+6\Big) + 2(z-3)\Big], \qquad z = \frac{r^2}{2(\sigma^2+R^2)}. \tag{2.22}$$

Again, the deduction of these equations is done separately in Appendix B. For both, ω_x^E and ω_y^E, if we focus our attention in the center of the image (where $r \to 0$, the terms tend to $\lambda(z,R) \to 0$, and $e^{-z} \to 1$),

we are left with:

$$\omega_x^E(0,\xi,\phi,R) = \frac{P}{16\pi^2}\frac{\sigma^2R^2}{\sigma^2+R^2}\cos 2\phi,$$
$$\omega_y^E(0,\xi,\phi,R) = \frac{P}{16\pi^2}\frac{\sigma^2R^2}{\sigma^2+R^2}\sin 2\phi. \tag{2.23}$$

Therefore, an estimation of the polarization angle can easily be computed through:

$$\hat{\phi}^E(\phi,R) = \frac{1}{2}\arctan\Big(\frac{\omega_y^E(0,\xi,\phi,R)}{\omega_x^E(0,\xi,\phi,R)}\Big). \tag{2.24}$$

As it would be expected, the wavelet coefficients ω_x^B and ω_y^B of the B-mode source profile look like 45° rotations of ω_x^E and ω_y^E, i.e.:

$$\omega_x^B(r,\xi,\phi,R) = \frac{P}{16\pi^2}\frac{\sigma^2R^2}{\sigma^2+R^2}\Big[-\sin 2\phi e^{-z} + \Big(\sin 4\xi\cos 2\phi - \cos 4\xi\sin 2\phi\Big)\lambda(z,R)\Big],$$
$$\omega_y^B(r,\xi,\phi,R) = \frac{P}{16\pi^2}\frac{\sigma^2R^2}{\sigma^2+R^2}\Big[\cos 2\phi e^{-z} - \Big(\cos 4\xi\cos 2\phi + \sin 4\xi\sin 2\phi\Big)\lambda(z,R)\Big], \tag{2.25}$$

and thus, the estimation of the polarization angle that can obtain from the wavelet coefficients of the B-mode is given by:

$$\hat{\phi}^B(\phi,R) = \frac{1}{2}\arctan\Big(\frac{-\omega_x^B(0,\xi,\phi,R)}{\omega_y^B(0,\xi,\phi,R)}\Big). \tag{2.26}$$

Now that we count with $\hat{\phi}^{E,B}$ estimations of the polarization angle, we can go back to equation (2.20) to reconstruct the E- and B-modes source profiles. A $\hat{P}$ estimation of the polarization intensity of the source can also be obtained by looking at the central point of the filtered image, since

$$\omega_{E,B}(0,\xi,\phi,R) = \frac{P}{16\pi^2}\frac{\sigma^2R^2}{\sigma^2+R^2}\cos 2\Big(\phi - \hat{\phi}^{E,B}(\phi,R)\Big). \tag{2.27}$$

Consequently, if the $\hat{\phi}^{E,B}$ determination is good enough such as $\phi - \hat{\phi}^{E,B} \approx 0$, then, an estimation of the polarization intensity can be simply computed as:

$$\hat{P}^{E,B}(\phi,R) = 16\pi^2\frac{\sigma^2+R^2}{\sigma^2R^2}\omega_{E,B}(0,\xi,\phi,R). \tag{2.28}$$

We count now with two independent estimations of the source polarization angle $\hat{\phi}^{E,B}$, and intensity $\hat{P}^{E,B}$, that, in principle, should give us similar values for the actual polarization angle ϕ and intensity P. However, in real life situations, where the backgrounds present in E-modes are much higher than those in B-modes, the results coming from filtering B-mode maps are expected to produce more accurate values for the polarization angle and intensity. Indeed, this fact alone is enough to justify the present study, since working in E- and B-modes also reports advantages with respect to the standard approach of working in Q and U maps [23] for the very same reasons.

2.3 Pixelization effects and calibration

All the equations presented in the previous section rely on continuous functions. However, in digital images the information is discretized into pixels, compromising the resolution of functions to the number of pixels

used. Therefore, the pixelization could affect the implementation of the filter and the accuracy of its results.

Since the filter is designed to operate in the plane, the sky region (initially observed on the sphere) where we want to apply it must be first projected onto the Cartesian plane. To guarantee that no significant distortions in the shape of point-like sources are introduced by projecting, projections are limited to $12.8° \times 12.8°$ square patches, where the flat approximation of the sphere's surface still holds and projected regions are large enough to have a good representation of the statistical properties of the microwave background. In addition, the size of the pixels in the plane should also be similar to the size of the pixels in the sphere for the projection to accurately preserve the information contained in each pixel. For the chosen patch size, if we want the pixels in our plane to have a similar size than the ones in the sphere pixelization, then the projected square in the plane must have a side of $\#\mathrm{pix}_{\mathrm{side}} = \mathrm{nside}/4$. Here nside is a specific parameter of the HEALPix pixelization [17], which is the one used in the context of the CMB science, that determines the number of pixels in which the sphere is divided, $\#\mathrm{pix}_{\mathrm{sphere}} = 12\mathrm{nside}^2$. The nside values are restricted to powers of two, therefore we will always have an even number of pixels in each side. Working with even sided squares has the advantage of allowing the use of the *Fast Fourier Transform*, though it also leaves us with no central pixel to take as coordinate origin. To solves this, $\#\mathrm{pix}_{\mathrm{side}}/2$ is defined as central pixel for both x and y axes.

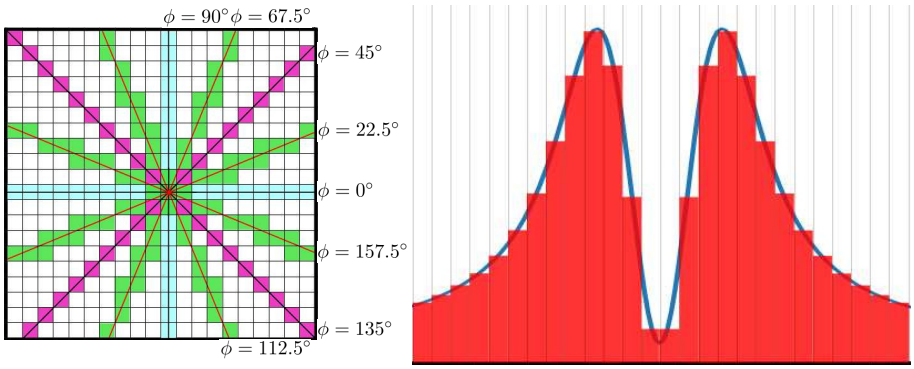

Figure 2.2: Limitations imposed by image pixelization in the filter resolution. Only sources with their lobes falling in the x or y axes or the diagonals, will suffer no distortion. Due to pixelization effects, all rest of the polarization angles will not be well defined. The sampling of the radial source profile is also limited by pixelization.

As shown in figure 2.2, the pixelization limits both, the angular and radial resolution of the source's profile. The compact nature of the source, limits its extension to the smallest r, where no matter how fine pixelization is, only $\theta = \{0°, 45°, 90°, 135°, 180°, 225°, 270°, 315°\}$ angles will be perfectly defined. In contrast, the angles right between these ones are the most affected by pixelization distortion. Therefore, for $\phi = \{0°, 45°, 90°, 135°\}$, when the lobes of the point-like source fall along the direction of the x and y axes and the diagonals, no error will be committed by the filter in the estimation of the polarization angle, but for polarization angles just in the middle, $\phi = \{22.5°, 67.5°, 112.5°, 157.5°\}$, the largest error is expected. These restrictions imposed by pixelization clearly manifest themselves in the determination of the polarization angle when applying the filter even to a naked source, as shown in figure 2.3. Since the estimation of the polarization intensity depends on the accuracy of the $\hat{\phi}^{E,B}$ determination like $\hat{P}^{E,B} \propto \cos 2(\phi - \hat{\phi}^{E,B})$, in turn, the largest errors in polarization intensity determination will be shifted to $\phi = \{0°, 45°, 90°, 135°\}$. In addition, the accuracy in the determination of P is also limited by how well the discrete points in the pixel grid reproduce the continuous function. Naively modeling this

discrepancy like $\hat{P}^{E,B} = P - \epsilon$, where the value of ϵ would decrease for progressively finer pixelization levels, and the error in the polarization angle determination simply like $A\cos 2\phi$, as the results seen in figure 2.3 suggest, the relative error commmitted in the determination of the polarization intensity would behave as:

$$\frac{P - \hat{P}^{E,B}}{P} \propto 1 - (1 - \frac{\epsilon}{P})\cos(2A\cos 2\phi). \tag{2.29}$$

Since ϵ/P is very small but different from zero, this toy model explains why the relative error in the determination of the polarization intensity seen in figure 2.3 shockingly does not oscillate around zero. Moreover, giving A and ϵ the actual values they present in these scenarios, the model precisely reproduces the relative errors displayed for the discrete polarization intensity up to 2π factor like $(1 - \frac{\epsilon}{P})\frac{1}{2\pi}$. This extra 2π factor was introduced at some point during the deduction of the expressions for the source's profile or the wavelet coefficients, possibly as a result of mixing different symmetric criterions of the Fourier transform. Nevertheless, it is just a constant factor that hereafter will be absorved whitin the calibration.

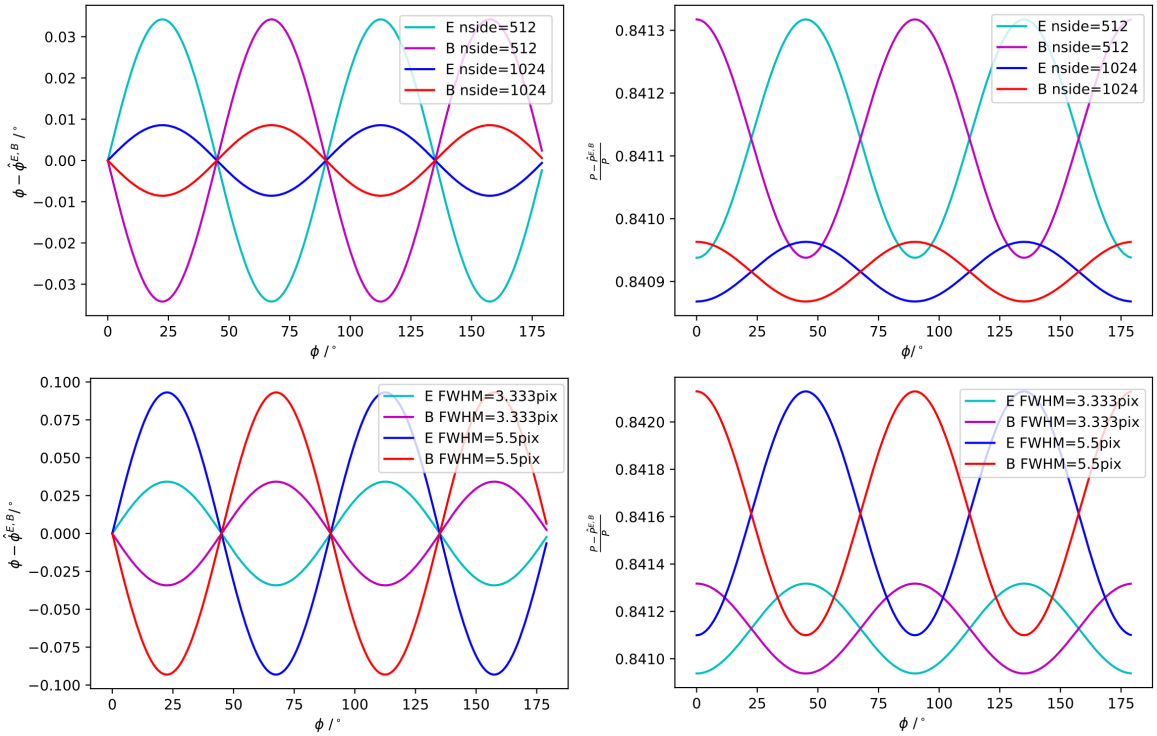

Figure 2.3: Errors introduced by the chosen pixelization and FWHM/pix ratio both, in the determination of the polarization angle ($\hat{\phi}^{E,B}$) and intensity ($\hat{P}^{E,B}$), when applying the filter to a naked source. The top panel displays how the accuracy improves when reducing the pixel size, effectively done by increasing the nside parameter, while the lower panel shows how, in contrast, a larger FWHM/pix ratio deteriorates it.

A finer pixelization allows for both, a better angular resolution and a more precise approximation of the value of the continuous functions at all points, decreasing the induced errors in the determination of polarization angle and intensity. Once pixelization is fixed, the only free parameter altering the resolution of the source's profile is the FWHM/pix ratio, or alternatively, σ/pix. An increase in the FWHM/pix ratio has the effect of smoothing the profile of the point-like source. As variations in the value of the source's profile are now smaller from pixel to pixel, the ability of the filter to distinguish from one polarization angle to another is also diminished. Therefore, increasing the FWHM/pix ratio aggravates the errors committed in the polarization intensity and the angle determination, as can be seen in the bottom panels

of figure 2.3. Albeit not ilustrated here, playing with the filter scale R has the same effect that increasing or decreasing the FWHM/pix ratio.

Since these errors in the polarization angle and intensity determination are exclusively caused by known parameters of image pixelization, filter definition and instrument resolution, they can be easily corrected. Multiplicative calibration functions suffice to correct the initial estimations of polarization intensity $\hat{P}^{E,B}$ and angle $\hat{\phi}^{E,B}$ given by the filter into their rightfull values $\tilde{\phi}^{E,B}$ and $\tilde{P}^{E,B}$ like:

$$\begin{aligned}\tilde{\phi}^{E,B} &= \hat{\phi}^{E,B}(\phi, R/\sigma, \text{nside}, \text{fwhm}) f^{E,B}(\hat{\phi}^{E,B}, R/\sigma, \text{nside}, \text{fwhm}),\\ \tilde{P}^{E,B} &= \hat{P}^{E,B}(\phi, R/\sigma, \text{nside}, \text{fwhm}) g^{E,B}(\hat{\phi}^{E,B}, R/\sigma, \text{nside}, \text{fwhm}),\end{aligned} \tag{2.30}$$

where the calibration functions $f^{E,B}$ and $g^{E,B}$ are obtained from the initial outputs and applying the filter to a naked source as:

$$\begin{aligned}f^{E,B}(\hat{\phi}^{E,B}, R/\sigma, \text{nside}, \text{fwhm}) &= \frac{\phi}{\hat{\phi}^{E,B}(\phi, R/\sigma, \text{nside}, \text{fwhm})},\\ g^{E,B}(\hat{\phi}^{E,B}, R/\sigma, \text{nside}, \text{fwhm}) &= \frac{P}{\hat{P}^{E,B}(\phi, R/\sigma, \text{nside}, \text{fwhm})}.\end{aligned} \tag{2.31}$$

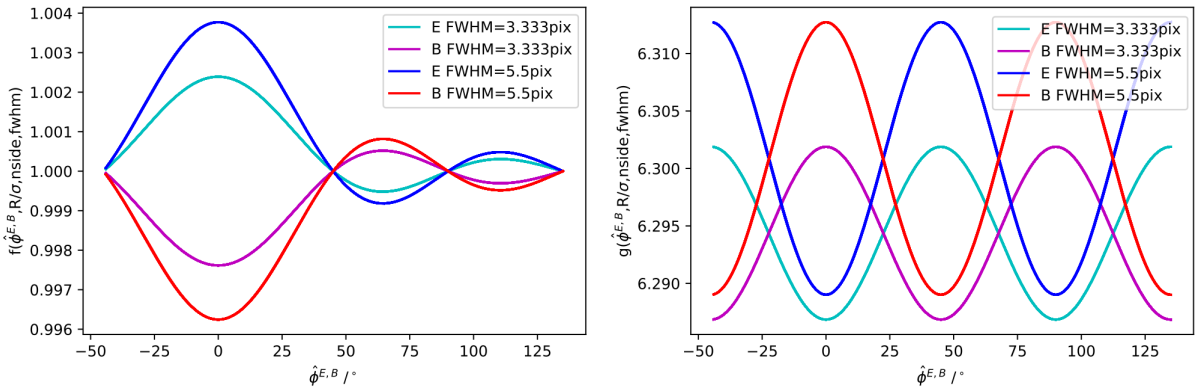

Figure 2.4: Examples of the calibration functions $f^{E,B}$ and $g^{E,B}$ used to correct the initial value obtained for the polarization angle and intensity, respectively. Calibration functions are shown for two different FWHM/pix ratio to illustrate how different pixelization levels affect their profiles.

An example of the resulting calibration functions is shown in figure 2.4. The atenuation observed in the angle calibration function $f^{E,B}$ is perfectly compatible with the previously seen profile of the error committed in polarization angle determination, since the same discrepancy in $\phi - \hat{\phi}^{E,B}$ will progressively yield a smaller relative error for larger polarization angles. In order to generate continuous angle calibration functions as the ones displayed, the output polarization angles coming from equations (2.24) and (2.26) that fall in the fourth quadrant are not moved to their rightful values. Under this conditions, polarization angles between $\phi \in [135°, 179°]$ are $\hat{\phi}^{E,B} - 180°$ shifted. After calibration, these angles are brought back to their rightful values. Calibration functions correcting polarization intensity $g^{E,B}$ oscillate around a $\sim 2\pi$ value, safetily collecting the extra 2π factor that previously was identified to exist in the filter definition equations.

Calibration functions have been computed and stored for later use for polarization angles $\phi \in [-44°, 135°]$ with a one degree step, filter scales between $R/\sigma \in [0.4, 2.15]$ with a 0.05 step and for the FWHM/pix and nside combinations that will be used later to test filter performance. For polarization

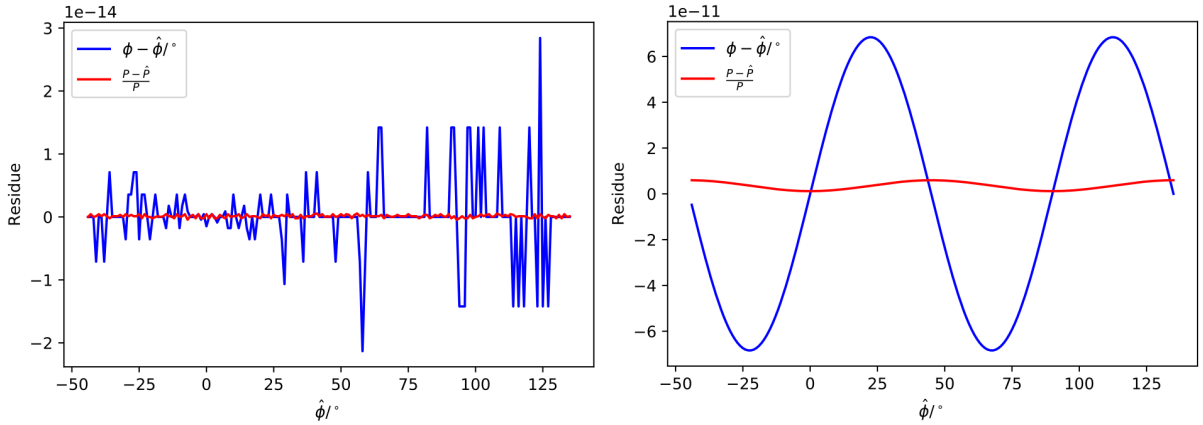

Figure 2.5: Residual error in polarization angle and intensity determination after calibration. The graph on the left shows the residual errors obtained for tabulated filter scales, while the graph on the right illustrates how for the non-tabulated filter scales that had to be interpolated, the remaining residues maintain the previously seen profile for the error in polarization angle and intensity determination.

angles and filter scales not tabulated, the value of the calibration function is interpolated using cubic splines. With the implemented interpolation function, the residual error in polarization angle $\tilde{\phi}^{E,B}$ and intensity $\tilde{P}^{E,B}$ left after calibration has an order of magnitude of 10^{-14} and 10^{-16}, respectively, as can be seen in figure 2.5. As the interpolation function defined does not perfectly reproduce calibration curves for not tabulated filter scales, the residual error present in those cases maintains the profiles previously seen in the determination of polarization angle and intensity, in the worst case, multiplied by a 10^{-10} factor.

2.4 Simulations description

With the filter now well defined and calibrated, its time to test its performance in real life situations, where point-like sources are laid upon a background of CMB's and foregrounds' emissions, and suffer from instrumental noise. The maps of the microwave sky used here were produced with the *Python Sky Model* (PySM), a software that simulates CMB and galactic foregrounds maps. PySM provides several models to simulate both, intensity and polarization, maps of the radiation coming from CMB, synchrotron, thermal dust, free-free and anomalous microwave emission. In these simulations, a gravitationally lensed CMB signal is also included. A detailed description of the different models PySM implements for each component, and the spectral laws used to calculate their emissions can be found in [28]. Figure 2.6 collects the intensity and the E- and B-mode polarization maps of foregrounds' emission obtained with PySM for the three frequency channels where the filter preformance will be tested. Like most microwave sky maps, PySM maps are presented in temperature units rather than in intensity. CMB temperature units δT_{CMB} definition is based in the blackbody $B(\nu, T)$ nature of CMB's spectrum. Tiny CMB temperature fluctuations δT around its mean temperature $\bar{T}$ can be expressed as a Taylor expansion like:

$$\delta B(\nu, \bar{T} + \delta T) \approx B(\nu, \bar{T}) + \left(\frac{\partial B(\nu, T)}{\partial T}\right)_{\bar{T}} \delta T, \tag{2.32}$$

where the constant term, or monopole, $B(\nu, \bar{T})$ is always removed. This way, the measured fluctuations in intensity δI_ν are transformed into temperature values as:

$$\delta T_{CMB}(\mu \mathrm{K_{CMB}}) \left(\frac{\partial B(\nu, T)}{\partial T}\right)_{\bar{T}} = \delta I_\nu (\mathrm{Jy/sr}). \tag{2.33}$$

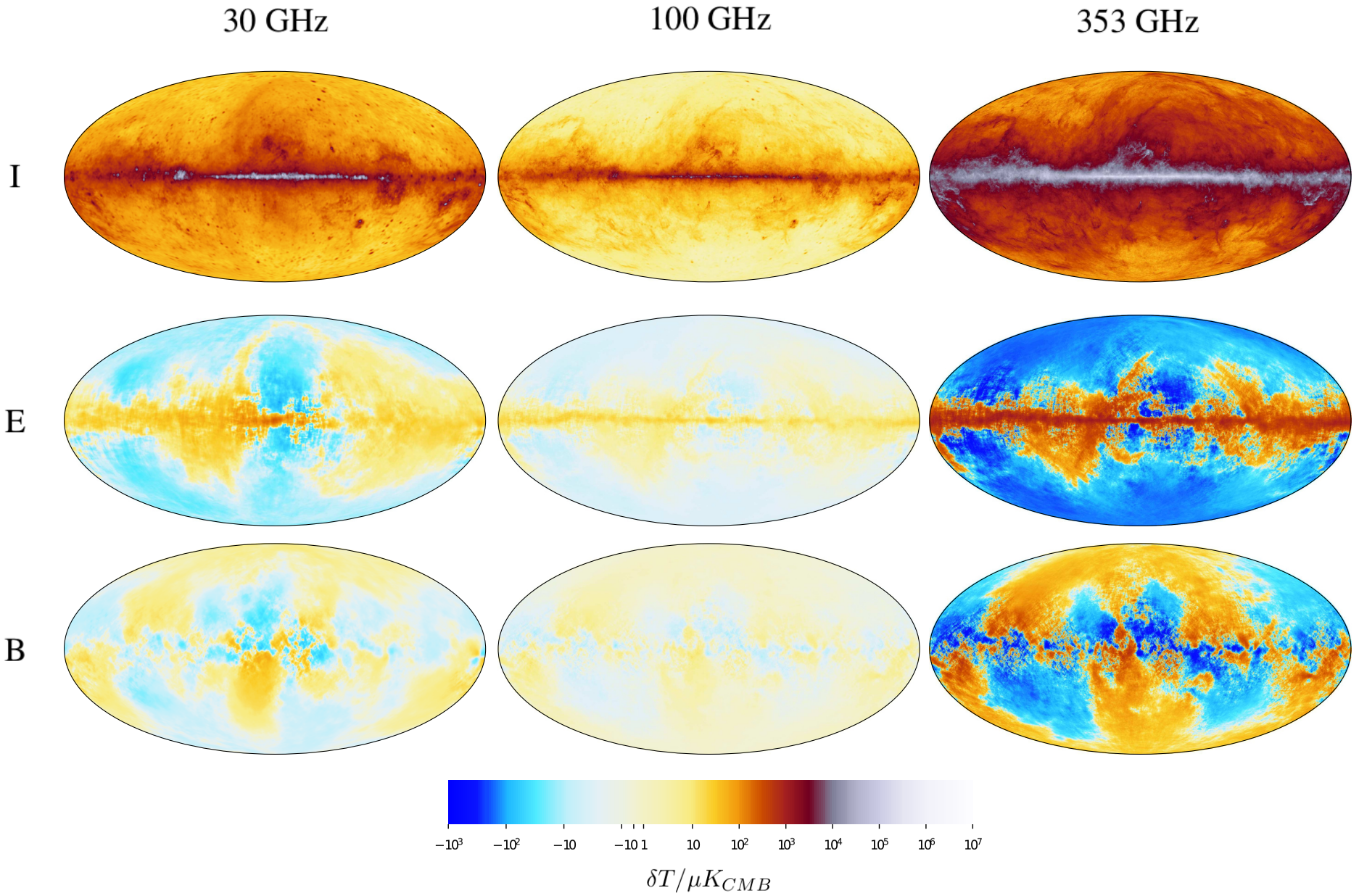

Figure 2.6: Intensity and E- and B-mode polarizations maps of foregrounds' emission produced by PySM for the frequency channels simulating three of the channels of the Planck satellite, in which the filter performance will be tested. To allow the comparison between the wide range of values foregrounds' emission present in the different channels, the Planck color scale [22] based on the inversion of the function $y = 10^x - 10^{-x}$ is adopted.

When working with $\mu\mathrm{K_{CMB}}$ for CMB's temperature units and intensity fluctuations in Jy/sr, the value of the conversion factor between them is frequency dependent and can be approximated [18] like:

$$\Big(\frac{\partial B(\nu,T)}{\partial T}\Big)_{\bar{T}} \approx 24.8\Big[\frac{x^2}{\sinh(x/2)}\Big]^2, \qquad x \approx \frac{\nu}{56.8}\mathrm{GHz}, \tag{2.34}$$

making CMB's temperature units frequency independent.

In order to evaluate the performance of the filter in as close to real conditions as possible, low, medium and high-frequency Planck channels will be simulated. Different levels of the instrumental noise, representing current and future experiments, will also be simulated. For each channel, the filter will be applied to point-like sources with $\delta I_\nu = \{0.3\mathrm{Jy}, 1\mathrm{Jy}, 10\mathrm{Jy}\}$ fluxes in intensity, where the 0.3 Jy value is choosen for being representative of the flux of the faintest sources currently detected [23]. We will assume our point-like sources to have a polarization fraction of $\pi = 0.3$, so the polarization intensity will be reduced to $P = \pi\delta I_\nu$. Since frequency channels also present a different resolution, in addition to the frequency dependent conversion factor between intensity and CMB's temperature units, we must take into account the different areas A^ν_{pix} of the pixels in each channel to compute the final value of P. This way, the polarization intensities to simulate would be

$$P = \frac{\pi\delta I_\nu}{A^\nu_{\mathrm{pix}}}\Big(\frac{\partial B(\nu,T)}{\partial T}\Big)_{\bar{T}}. \tag{2.35}$$

This value is actually the total polarization intensity integrated over the whole source. However, since point-like sources posses a compensated profile, integrating over the whole source would give a null value. For this reason, in what is left of the chapter, we will express polarization intensity using the maximun value the source's profile presents at its positive lobes, P_{peak}. Quantifying the intensity of the point-like source like this, it becomes very intuitive to tell when the source will peak above the background signal and when it will be obscured by it.

Planck channels			Patch pixelization		
ν/GHz	nside	FWHM/arcmin	patch side/pix	pixel size/arcmin	FWHM/pix
30	512	33	128	6	5.5
100	1024	10	256	3	3.333
353	2048	5	512	1.5	3.333

Table 2.1: nside of the sphere pixelization and detector FWHM that characterize Planck's 30 GHz, 100 GHz and 353 GHz channels [22], and the parameters of the implemented patch needed to emulate them.

ν/GHz	$P_{peak,i}/\mu\mathrm{K_{CMB}}/\mathrm{arcmin}$	$\sigma_{n,i}/\mu\mathrm{K_{CMB}}/\mathrm{arcmin}$
30	0.166, 0.555, 5.547	210, 50, 5
100	0.204, 0.681, 6.814	120 ,50, 5
353	0.658, 2.194, 21.941	440, 50, 5

Table 2.2: Polarization intensity $P_{peak,i}$ describing the maximun values the simulated point-like sources take at their positive lobes and standard deviations characterizing the different levels of white Gaussian noise used ($\sigma_{n,i}$). Highest noise level is representative of the Planck data [22], while the lower ones are expected for future missions. Subindexes $i = 1, 2, 3$ identify the different polarization intensities and noise levels in the same order in which they appear here. Therefore, for $i = 1$ we have the highest noise level and the faintest source, and for $i = 3$, the lowest noise level and the brightest source.

As can be observed in figure 2.6, polarization appreciably varies for different regions of the sky and from one frequency channel to another. Consequently, to accurately evaluate the performance of the filter, the filter must be applied in different regions of the sky. For this purpose, the microwave

sky will be divided into three characteristic regions based on the intensity of foregrounds' emission. To ensure that we count with all kind of foregrounds' emissions in the plane patches where the filter will be applied, we project 768 $12.8^\circ \times 12.8^\circ$ regions of the sky, taking the positions of HEALPix $\mathrm{nside} = 8$ pixels as their centers. The downside of this sampling strategy is that most of the patches overlap in the sky at some point or another. The three distinct regions of the microwave sky will now be independently defined for the E- and B-mode and at each frequency channel, based on the dispersion ($\sigma_{patches}$) that the foregrounds' emission presents in these projected patches. As the histogram in figure 2.7 exemplifies, patches of low dispersion are the most common. Motivated by this distribution, the dispersion ranges defining zones I, II and III seen in table 2.3 are set so that approximately 40%, 30% and 27% of the initial patches, respectively fall into each zone. The remaining 3% of the patches are dismissed for having especially high dispersions that do not seem to be very common in the microwave sky.

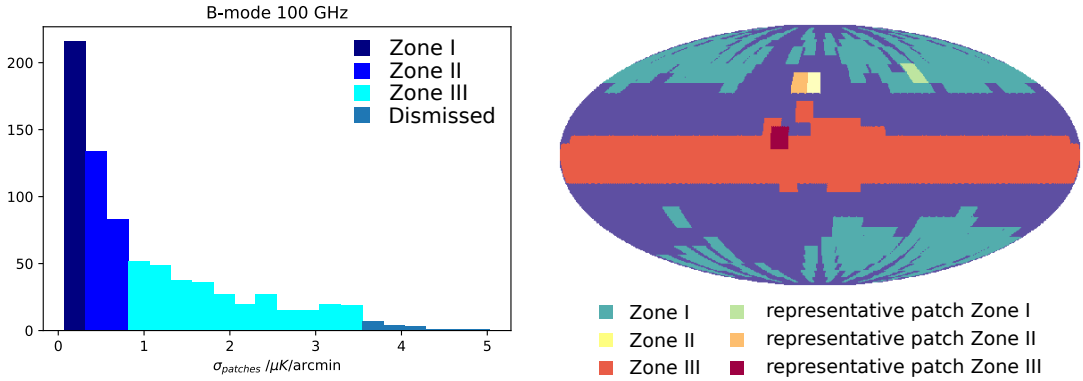

Figure 2.7: Left panel: Histogram displaying the distribution the dispersion of foregrounds' emission presents in the 768 distinct $12.8^\circ \times 12.8^\circ$ regions projected from the B-mode map at 100 GHz. Right panel: Distribution in the sky of the 166, 2 and 31 patches common to all frequency channels and to E- and B-mode maps that don't overlap at any point in the sky for zones I, II and III respectively. The patch selected to represent each of them is highlighted in a different color. This image has the same pixelation of the 30 GHz channel.

		$\sigma_{patches}$ /μK$_{\mathrm{CMB}}$/arcmin		
		30GHz	100 GHz	353 GHz
E	CMB-only	[1.11, 1.21]	[3.69, 3.83]	[5.16, 5.29]
	Zone I	[0.70, 5.55]	[0.08, 0.64]	[4.52, 31.43]
	Zone II	[5.55, 15.25]	[0.64,1.75]	[31.43, 85.24]
	Zone III	[15.25, 44.36]	[1.75, 8.42]	[85.24, 381.21]
B	CMB-only	[0.08, 0.09]	[0.21, 0.23]	[0.30, 0.31]
	Zone I	[0.33, 1.82]	[0.07, 0.32]	[3.74, 17.81]
	Zone II	[1.82, 4.78]	[0.32, 0.81]	[17.81, 45.93]
	Zone III	[4.78, 19.61]	[0.81, 3.54]	[45.93, 172.50]

Table 2.3: Range of the projected patches' dispersion that defines the three representative regions of the microwave sky, and the hundred CMB realizations at 1σ where the performance of the filter will be tested. Note that the values of CMB's dispersion change from one channel to the other due to the different resolution of each channel. The larger amplitude of E-modes both, in CMB's and foregrounds' emissions, becomes quite noticeable looking at the dispersion values.

As an extra constrain to make the defined regions coherent for all channels, we have also required patches in each zone to be common to E- and B-modes, and to the three different frequencies, and to not overlap with any other patch. This constraint leaves us with 166, 2 and 31 patches from zones I to III respectively, and from them, one patch is chosen to represent the characteristic foregrounds' emission of each region. The properties of the representative patches chosen for each region are collected in tables 2.4 and 2.5. Is in these representative patches where point-like sources of the desired properties and the

representative patch		σ_{patch}/ μK$_{\rm CMB}$/arcmin 30GHz	100 GHz	353 GHz
E	Zone I	2.247	0.428	19.761
	Zone II	6.859	0.651	33.693
	Zone III	30.060	4.051	195.248
B	Zone I	1.592	0.196	9.480
	Zone II	3.587	0.415	21.914
	Zone III	12.541	2.377	130.938

Table 2.4: Dispersion of the representative patches chosen to illustrate foregrounds' emission on each Zone.

	representative patch location longitude /°	latitude /°
Zone I	[-90.0, -77.2]	[41.7, 54.5]
Zone II	[10.5, 23.3]	[35.4, 48.2]
Zone III	[21.7, 34.5]	[3.2, 16.0]

Table 2.5: Coordinates specifying the position in the sky of the $12.8^\circ \times 12.8^\circ$ representative patches chosen to illustrate foregrounds' emission in each Zone.

white Gaussian noise used to simulate instrumental noise would be added, to test the filter performance. Using the sampling strategy previously described, 768 realizations of the CMB radiation were obtained. Based on their dispersion, a hundred of them at a 1σ were selected to be added to the representative patches of foregrounds' emission, in order to consider the E- and B-modes introduced by the CMB. For completeness, the filter performance will also be tested in this ideal CMB-only situation.

2.5 Test of the filter performance

The accuracy of the performance of the filter in each of the previously defined regions of the sky is statistically determined using a hundred different realizations of instrumental noise and CMB realizations at 1σ. A different realization of white Gaussian noise is coupled with every one of the hundred patches of E- and B-mode CMB radiation. When testing in zones I to III, the patch of foregrounds' emission characterizing each zone is added to this CMB+noise mix. This leaves us with one hundred patches per sky region. In every one of them, thirty-six different point-like sources of polarization angles between $\phi \in [0^\circ, 180^\circ)$ with a 5° step are added each time, to the center of the map. The designed filter (with a filter scale of $R/\sigma = 1$) is then applied to recover the polarization angle and intensity in each of the described cases. In this way, for every polarization angle explored we count with a hundred different reponses for $\tilde{\phi}^{E,B}$, and for every polarization intensity collected in table 2.2, 3600 outputs for $\tilde{P}^{E,B}_{peak}$.

The characterization of the error associated to the determination of the polarization angle, $\sigma^{E,B}_{\phi}(\phi)$, is estimated through the standard deviation of the error $\Delta\phi^{E,B}_{patch}(\phi) = \phi - \tilde{\phi}^{E,B}_{patch}(\phi)$ committed in each realization. The same is done for the polarization intensity, where $\sigma^{E,B}_{P}(\phi)$ is the standard deviation of the relative error committed in each patch, $\Delta P^{E,B}_{patch}(\phi) = [P_{peak} - \tilde{P}^{E,B}_{peak,patch}(\phi)]/P_{peak}$. However, since the thirty-six polarization angles evaluated return an estimation of the same P value, this time the final estimation of the error of the polarization intensity is obtained averaging over all input angles: $\sigma^{E,B}_{P} =< \sigma^{E,B}_{P}(\phi) >_{\phi}$. In the following graphs, the filter accuracy recovering the input polarization angle is presented by plotting the recovered polarization angle averaged over all patches ($\Phi^{E,B}(\phi) \equiv< \tilde{\phi}^{E,B}(\phi) >_{patches}$) versus each input ϕ, with the corresponding error ($\sigma^{E,B}_{\phi}(\phi)$). In turn, to illustrate the accuracy of the polarization intensity determination, the recovered $\tilde{P}^{E,B}_{peak}$ averaged over all patches and then over all input angles ($\mathcal{P}^{E,B}_{peak} \equiv< \tilde{P}^{E,B}_{peak} >_{patches,\phi}$), is plotted versus the input $P^{E,B}_{peak}$, with the corresponding uncertainty ($\sigma^{E,B}_{P}$).

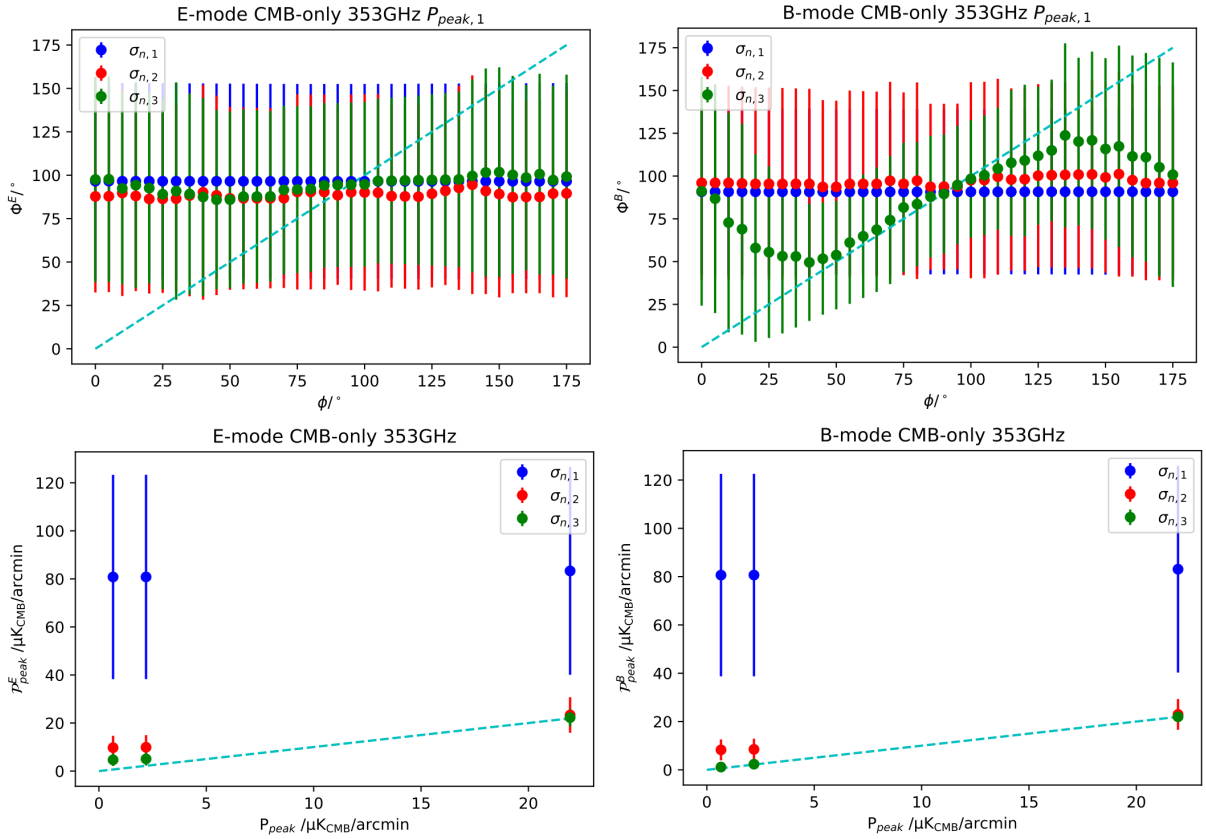

Figure 2.8: Example of the accuracy in the determination of the polarization angle and intensity achieved by the filter in the ideal situation of having only CMB and instrumental noise emissions. For low enough levels of noise, and operating in the B-mode map, the filter is able to recover the polarization angle for the faintest source simulated, even when counting with the larger CMB signal as background (i.e., operating in high resolution maps). In turn, the polarization intensity could only be correctly retrieved for large fluxes.

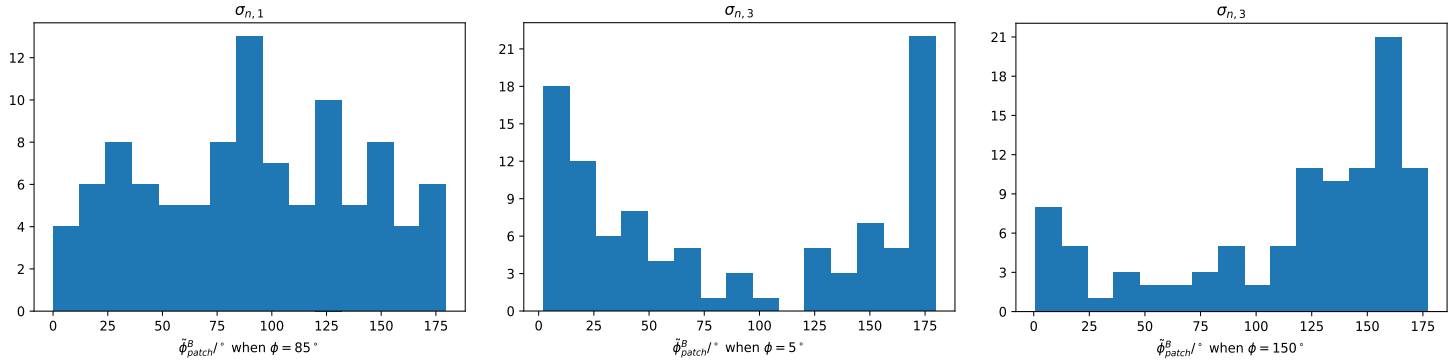

Figure 2.9: Histograms showing the different values for the polarization angle $\tilde{\phi}^B_{patch}$ returned by the filter, in each one of the realizations where a point-like source with a given polarization angle ϕ was added. These histograms correspond to some of the different noise levels and input polarization angles of the data shown for the B-mode in figure 2.8. The homogeneous distribution of the different $\tilde{\phi}^B_{patch}$ in the histogram on the left explains why the filter yields a 90° output when the source is obscured by the noise. The histograms on the right and center of the image show the effect the periodicity of the $[0°, 180°)$ interval has in the values of the recovered $\tilde{\phi}^B_{patch}$.

In the ideal situation of having only CMB's emission, the polarization angle and intensity of the faintest sources can be recovered in the B-mode maps if the instrumental noise is low enough, as can be seen in figure 2.8. The larger amplitude of the E-mode CMB map, obscures the point-like sources in E-mode maps, making undetectable the polarization angle, although the polarization intensity is still retrievable for brigth sources and low noise levels. Instrumental noise, as it consists of uncorrelated

random values abruptly varying from one pixel to the other, presents the most harmful effect to the performance of the filter. In contrast, the mostly homogeneous CMB background, only having smooth variations across the projected patches, does not suppose a big problem to the filter, for the B-mode maps.

When the filter is not able to recover the polarization angle, as happens for almost all noise levels in figure 2.8, $\Phi^{E,B}(\phi)$ just points to the average of the range of possible values $\phi \in [0°, 180°)$. In situations like these, as the histrogram on the left of figure 2.9 illustrates, the filter yields random outputs when applied to the different patches, that in average end up in a 90° polarization angle. The apparently worst result that the filter shows at small and large angles is, in turn, consequence of the periodicity of the interval of values ϕ takes. Due to the 180° rotational symmetry of point-like sources, polarization angles $\phi' = \phi \pm \pi$ shifted are indistinguishable. In such manner, the filter sometimes returns polarization angles around 180° for input angles near 0° and vice-versa. This behavior manifests itself in the central and right histograms of figure 2.9 and causes $\Phi^{E,B}(\phi)$ to gravitate towards values larger than the correct one for small angles, and towards smaller values than the correct one for large angles. To prevent these effects from wrongly estimate the error in the polarization angle, the final error associated to the determination of the polarization angle will be characterized from the 90°, $\sigma_\phi^{E,B} = \sigma_\phi^{E,B}(90°)$, as that is the angle whose histogram is less affected by the periodicity of the interval. The periodicity of the range of possible values for the polarization angle must also be considered at the time of interpreting the meaning of this $\sigma_\phi^{E,B}$ error. For example, in the scenario described in the histogram in the right of figure 2.8, the most probable angle would be $\tilde{\phi}^B = 159°$, and since the estimated error is $\sigma_\phi^B = 35°$, this $\tilde{\phi}^B$ value would also be compatible with any angle between $[0°, 14°] \cup [124°, 180°)$.

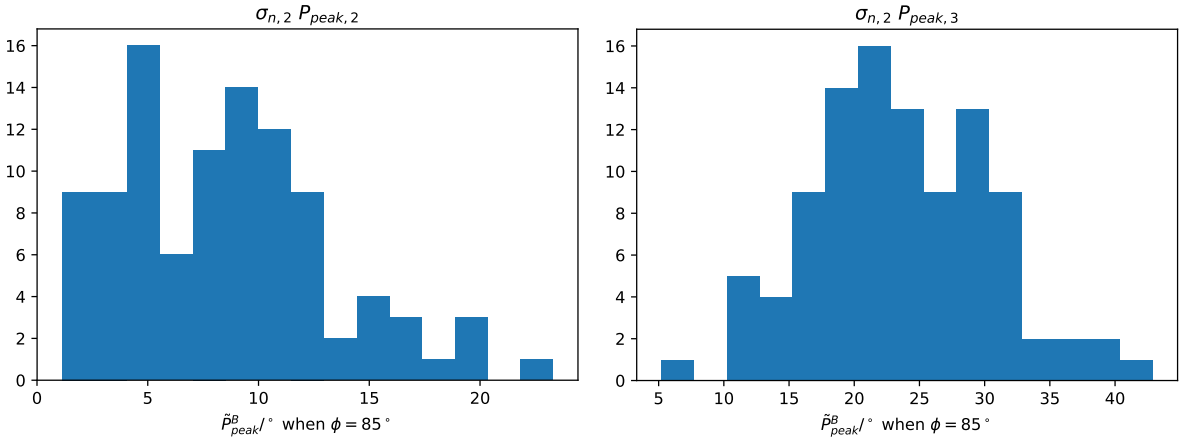

Figure 2.10: Histograms showing the different values for the polarization intensity $\tilde{P}^B_{patch}$ returned by the filter, in each one of the realizations where a point-like source with a given polarization angle ϕ was added. These histograms correspond to the polarization intensities $P_{peak,2}$ and $P_{peak,3}$, and the noise level $\sigma_{n,2}$, of the data shown for the B-mode in figure 2.8. For high polarization intensities, the different values returned for P_{peak}, are uniformly spread towards larger and smaller values around the input P_{peak}. However, since polarization intensity is a positive defined magnitude, for low polarization intensities, the distribution of returned valuas is skewed to the rigth, and in average produces a polarization intensity larger than the input one.

In turn, the nature of the polarization intensity also affects the plots of the recovered $\mathcal{P}^{E,B}_{peak}$ versus the input P_{peak}. As displayed in the histogram on the right of figure 2.10, for high polarization intensities, the different values recovered by the filter in each realization are distributed around the input P_{peak}, spreading uniformly towards larger and smaller values. However, since polarization intensity is a positive defined magnitude, when dealing with small intensities, the possible values for the polarization intensity are

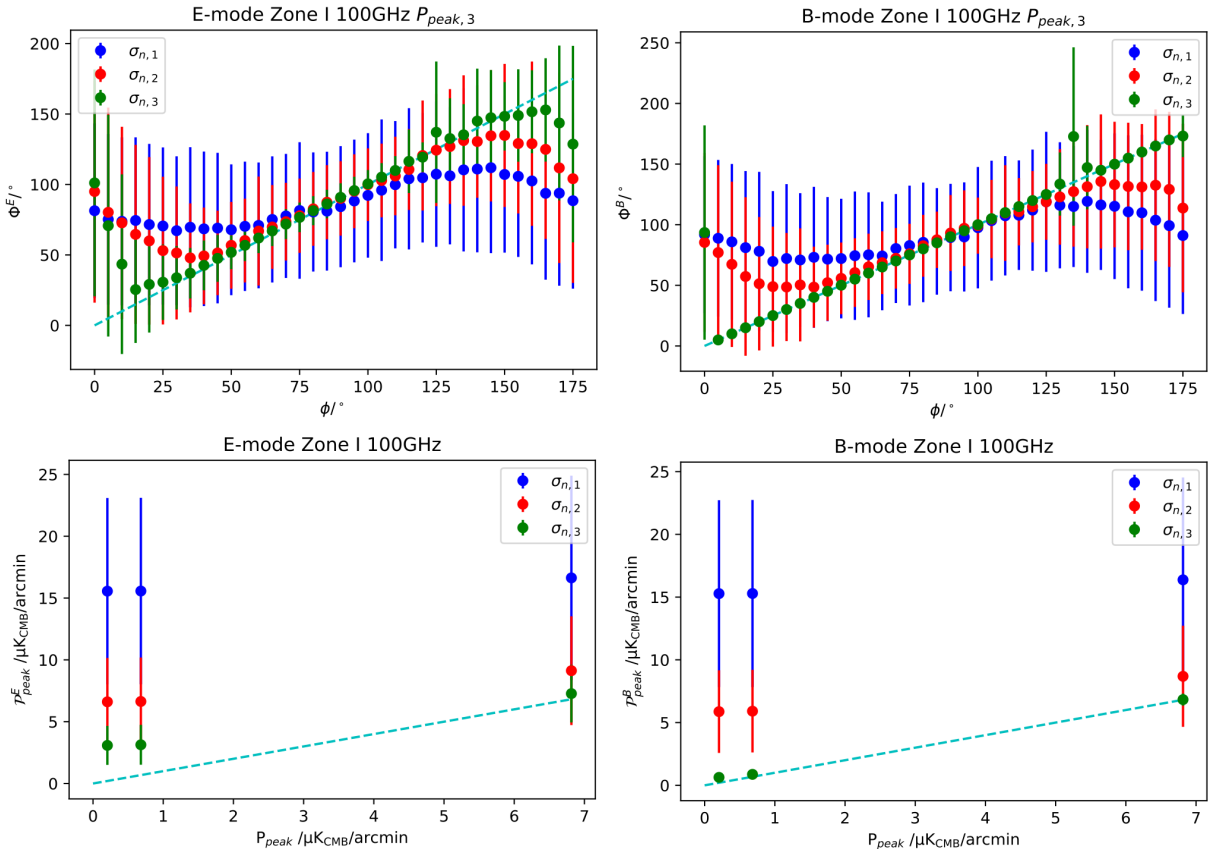

Figure 2.11: In the presence of foregrounds' emission, but with CMB radiation still being the dominant background, the filter is able to recover the polarization angle even for high levels of noise if the source is brigth enough. In contrast, a good determination of the polarization intensity is only possible for the lowest noise level.

limited. Therefore, the distribution of the recovered values is skewed towards larger values of P_{peak} (histogram on the left of figure 2.10). This asymmetric distribution results in an average value that overestimates the real polarization intensity. Instrumental noise broadens the distribution of returned values, also skewing their distribution towards larger polarizations intensities when the statistical fluctuations are high enough. For this reason, when dealing with small polarization intensities or high noise levels, the estimated $\mathcal{P}^{E,B}_{peak}$ tends to be larger than the input value. Hence, plateauing above the dashed line is the telltale sign that indicates when the background and noise levels are too hight to allow the determination of the polarization intensity, same as yielding an average $\Phi^{E,B} = 90^\circ$ is for the polarization angle. Therefore, to correctly characterize the fondness of the polarization intensity determination, we must give an estimate of this bias (b_P) along with the estimation of the committed error. For coherence, we will define the final error committed in the polarization intensity as the one made at 90°, $\sigma_P^{E,B} = \sigma_P^{E,B}(90^\circ)$, like we did for the polarization angle. $\sigma_P^{E,B}(\phi)$ only presents a very small dependency with the input polarization angle, induced rather by the particular anisotropies of the single patch of foregrounds' emission, where the filter was tested, than by any intrinsic property of the filter itself, so the values of $\sigma_P^{E,B}$ and $\sigma_P^{E,B}(90^\circ)$ are compatible. This way, our criterion to establish a detection will imply that $b_P < \sigma_P^{E,B}$.

For regions where the CMB signal stands above the foregrounds' emission like the one displayed in figure 2.12, the filter is capable of recovering the polarization angle, even for high levels of noise when point-like source are brigth enough to peak above CMB's emission. However, polarization intensity detection is only possible for the lowest noise level. The plots displayed in figures 2.8 and 2.12 make

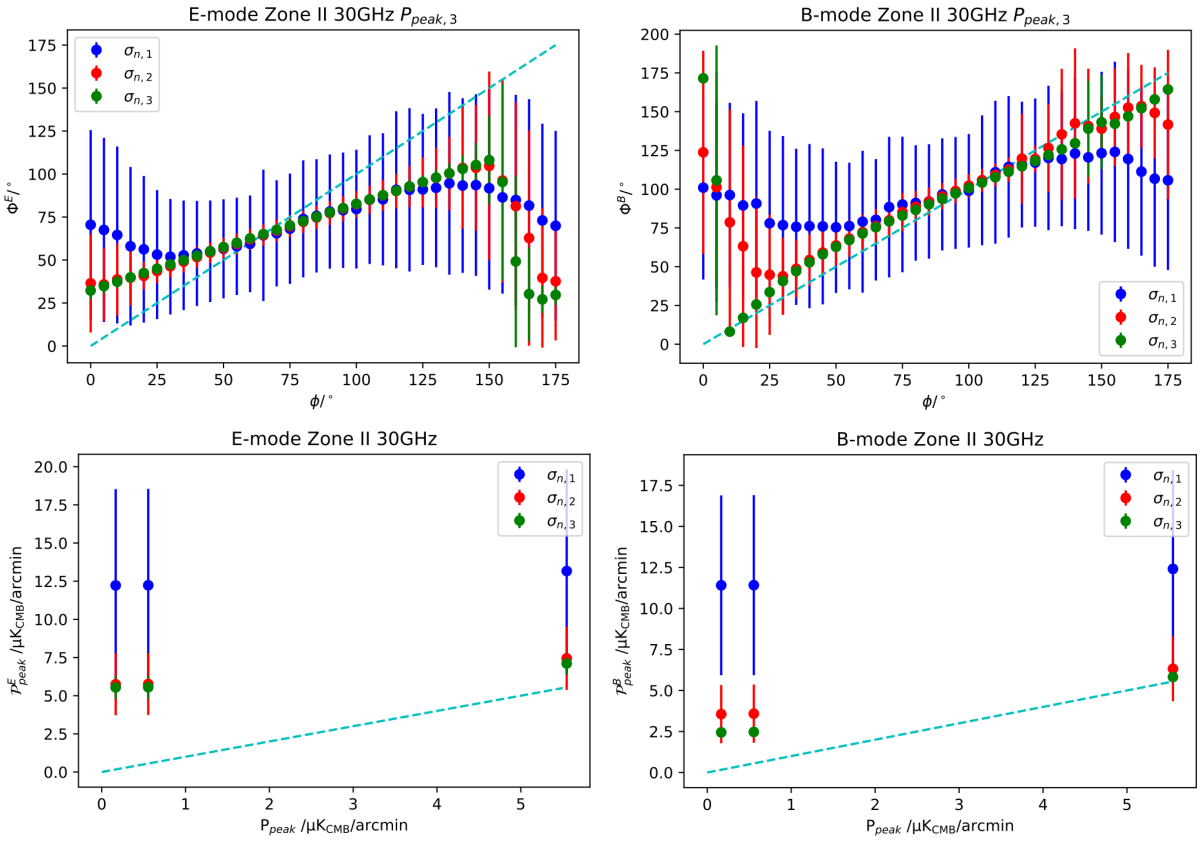

Figure 2.12: Working with B-mode maps, it is possible to recover the polarization angle and intensity of bright sources for the $\sigma_{n,2}$ and $\sigma_{n,3}$ levels of noise even when foregrounds radiation is the dominant emission. In contrast, the results obtained from the E-mode maps of the same region, are severely biased.

evident how, when dealing with the E- and B-mode counterparts of the same map, the lower amplitude of the B-modes from CMB and foregrounds emissions, allow for a better determination of the properties of point-like sources. This affirmation holds even in regions where foregrounds' emissions dominate, as happens in the scenario shown in figure 2.12, where the polarization angle and intensity of bright sources are recovered for the $\sigma_{n,2}$ and $\sigma_{n,3}$ noise levels in the B-mode map, but measurements done in the E-mode map are severely biased.

Table 2.6 collects the values of $\sigma_\phi^{E,B}(90°)$ and $b_P \pm \sigma_P^{E,B}(90°)$ obtained in every scenario considered, as a final summary of the test on filter performance. Highlighted cells, in blue for the E-mode, and in pink for the B-mode, show where detections where made (i.e., $b_P < \sigma_P^{E,B}$ under our criterion). As a general rule, in the presence of the same instrumental noise and for point-like sources of the same flux, more detections were possible when working with the B-mode map. A comparison cell by cell of the E- and B-mode counterparts of each scenario, also shows that smaller errors and biases are associated to the B-modes. In conclusion, better results where obtained when working in B-mode maps, which is the confirmation of the initial motivation when planning this research project.

		$\sigma_{n,1}$			$\sigma_{n,2}$			$\sigma_{n,3}$			
	ν /GHz	$P_{peak,1}$	$P_{peak,2}$	$P_{peak,3}$	$P_{peak,1}$	$P_{peak,2}$	$P_{peak,3}$	$P_{peak,1}$	$P_{peak,2}$	$P_{peak,3}$	
CMB	30	59.9 ; 11.2 ± 5.5	59.2 ; 10.8 ± 5.5	43.5 ; 6.2 ± 6.2	61.7 ; 2.6 ± 1.5	49.8 ; 2.2 ± 1.5	13.6 ; 0.1 ± 2.0	48.7 ; 0.7 ± 0.5	44.3 ; 0.5 ± 0.6	4.0 ; 0.0 ± 0.7	E
	100	53.6 ; 15.4 ± 7.5	57.6 ; 14.9 ± 7.5	43.3 ; 9.4 ± 8.2	59.4 ; 6.4 ± 3.5	48.2 ; 5.9 ± 3.5	26.8 ; 2.3 ± 4.3	49.4 ; 2.9 ± 1.6	46.6 ; 2.5 ± 1.6	10.1 ; 0.6 ± 2.4	
	353	56.1 ; 80.1 ± 42.6	55.6 ; 78.6 ± 42.8	54.1 ; 60.9 ± 45.8	51.7 ; 9.0 ± 5.0	56.3 ; 7.6 ± 5.1	10.2 ; 1.1 ± 7.5	47.3 ; 4.0 ± 2.6	44.9 ; 2.9 ± 2.7	4.9 ; 0.4 ± 3.7	
Zone I	30	48.9 ; 11.2 ± 5.8	53.0 ; 10.9 ± 5.9	36.8 ; 7.3 ± 6.9	26.6 ; 3.6 ± 1.9	23.5 ; 3.5 ± 1.9	8.2 ; 2.9 ± 2.0	7.0 ; 3.1 ± 0.7	6.3 ; 3.1 ± 0.7	2.5 ; 3.0 ± 0.7	
	100	58.0 ; 15.3 ± 7.5	52.8 ; 14.8 ± 7.5	43.0 ; 9.4 ± 8.2	49.8 ; 6.4 ± 3.5	47.8 ; 6.0 ± 3.5	26.4 ; 2.4 ± 4.3	48.4 ; 2.9 ± 1.6	45.5 ; 2.5 ± 1.6	9.9 ; 0.7 ± 2.4	
	353	58.9 ; 81.6 ± 42.4	58.5 ; 80.1 ± 42.7	57.3 ; 62.7 ± 45.9	48.7 ; 12.9 ± 6.8	38.3 ; 11.6 ± 6.9	9.0 ; 4.5 ± 7.7	22.1 ; 9.9 ± 3.5	34.4 ; 8.8 ± 3.6	4.3 ; 3.6 ± 3.7	
Zone II	30	49.9 ; 12.0 ± 6.3	49.3 ; 11.8 ± 6.4	33.2 ; 8.3 ± 7.4	13.5 ; 5.7 ± 2.0	12.8 ; 5.5 ± 2.0	7.0 ; 4.4 ± 2.0	3.8 ; 5.5 ± 0.7	3.6 ; 5.4 ± 0.7	2.1 ; 4.5 ± 0.7	
	100	57.4 ; 15.4 ± 7.5	52.1 ; 14.9 ± 7.5	41.8 ; 9.5 ± 8.3	48.1 ; 6.4 ± 3.5	51.4 ; 6.0 ± 3.5	25.2 ; 2.6 ± 4.4	46.2 ; 2.9 ± 1.7	42.9 ; 2.6 ± 1.8	9.5 ; 1.0 ± 2.4	
	353	54.0 ; 82.2 ± 45.9	57.7 ; 80.9 ± 46.2	42.6 ; 67.4 ± 50.3	10.0 ; 22.6 ± 7.5	9.3 ; 22.5 ± 7.5	5.1 ; 22.0 ± 7.5	4.8 ; 22.0 ± 3.7	4.5 ; 22.0 ± 3.7	2.5 ; 21.8 ± 3.7	
Zone III	30	22.3 ; 26.5 ± 8.4	29.3 ; 26.2 ± 8.4	10.1 ; 23.7 ± 8.3	2.3 ; 26.0 ± 2.3	2.3 ; 25.8 ± 2.3	2.1 ; 23.4 ± 2.2	0.8 ; 26.1 ± 0.7	0.8 ; 25.9 ± 0.7	0.7 ; 23.6 ± 0.7	
	100	51.8 ; 15.2 ± 7.6	55.6 ; 14.8 ± 7.6	46.7 ; 9.8 ± 8.5	41.3 ; 6.9 ± 3.8	39.8 ; 6.6 ± 3.8	20.7 ; 3.7 ± 4.6	45.2 ; 4.0 ± 2.0	33.1 ; 3.7 ± 2.1	7.9 ; 2.4 ± 2.4	
	353	33.3 ; 135.6 ± 54.1	33.3 ; 134.6 ± 54.1	32.6 ; 123.2 ± 54.5	1.9 ; 107.3 ± 8.3	1.9 ; 106.5 ± 8.3	1.7 ; 96.6 ± 8.3	1.0 ; 106.6 ± 3.7	1.0 ; 105.7 ± 3.7	0.9 ; 96.0 ± 3.7	
CMB	30	52.8 ; 11.0 ± 5.5	56.3 ; 10.6 ± 5.5	46.7 ; 6.4 ± 5.7	54.9 ; 2.5 ± 1.5	51.2 ; 2.1 ± 1.5	13.1 ; 0.4 ± 2.1	35.3 ; 0.1 ± 0.2	11.7 ; 0.0 ± 0.2	1.1 ; 0.0 ± 0.2	B
	100	55.4 ; 15.0 ± 7.4	54.6 ; 14.5 ± 7.5	44.3 ; 8.8 ± 8.1	51.3 ; 5.7 ± 3.3	49.3 ; 5.2 ± 3.3	31.4 ; 1.8 ± 4.1	42.5 ; 0.4 ± 0.3	24.9 ; 0.2 ± 0.4	2.0 ; 0.0 ± 0.5	
	353	48.2 ; 80.0 ± 41.9	52.5 ; 78.7 ± 41.8	46.9 ; 67.7 ± 41.4	48.4 ; 7.6 ± 4.4	44.0 ; 6.4 ± 4.7	8.0 ; 1.7 ± 6.9	34.9 ; 0.5 ± 0.6	10.2 ; 0.2 ± 0.8	1.0 ; 0.0 ± 0.8	
Zone I	30	58.5 ; 11.0 ± 5.6	53.5 ; 10.6 ± 5.5	42.8 ; 6.2 ± 5.7	54.3 ; 2.6 ± 1.4	51.0 ; 2.1 ± 1.5	14.6 ; 0.0 ± 2.0	5.0 ; 1.0 ± 0.2	5.1 ; 0.6 ± 0.2	1.2 ; −0.3 ± 0.2	
	100	55.4 ; 15.0 ± 7.4	54.6 ; 14.5 ± 7.5	44.3 ; 8.8 ± 8.1	51.1 ; 5.7 ± 3.3	49.2 ; 5.2 ± 3.3	31.3 ; 1.8 ± 4.1	41.1 ; 0.4 ± 0.3	24.1 ; 0.2 ± 0.4	2.0 ; 0.0 ± 0.5	
	353	51.7 ; 80.6 ± 41.1	51.2 ; 79.3 ± 41.0	59.3 ; 64.6 ± 40.7	42.0 ; 10.3 ± 4.8	34.9 ; 9.2 ± 5.0	7.3 ; 4.2 ± 6.7	3.4 ; 6.3 ± 0.8	3.1 ; 5.4 ± 0.8	0.9 ; 2.5 ± 0.8	
Zone II	30	47.5 ; 11.3 ± 5.5	51.3 ; 10.9 ± 5.5	36.2 ; 7.4 ± 6.2	40.1 ; 3.5 ± 1.8	25.4 ; 3.3 ± 1.8	8.5 ; 2.6 ± 2.2	2.4 ; 2.4 ± 0.2	2.1 ; 2.4 ± 0.2	0.8 ; 2 ± 0.2	
	100	59.3 ; 15.0 ± 7.5	54.3 ; 14.5 ± 7.5	44.0 ; 8.8 ± 8.2	54.9 ; 5.7 ± 3.3	48.5 ; 5.2 ± 3.3	21.9 ; 2.0 ± 4.1	34.3 ; 0.5 ± 0.3	19.7 ; 0.3 ± 0.4	1.9 ; 0.2 ± 0.5	
	353	51.3 ; 80.7 ± 41.3	50.8 ; 79.5 ± 41.2	46.0 ; 65.1 ± 41.1	46.9 ; 9.5 ± 5.0	34.1 ; 8.7 ± 5.3	6.6 ; 5.7 ± 6.8	4.1 ; 5.0 ± 0.8	3.3 ; 4.8 ± 0.8	0.9 ; 4.1 ± 0.8	
Zone III	30	19.8 ; 18.8 ± 7.7	19.2 ; 18.7 ± 7.8	13.2 ; 18.0 ± 8.3	3.1 ; 17.2 ± 2.3	3.1 ; 17.2 ± 2.3	2.4 ; 17.2 ± 2.3	0.4 ; 17.1 ± 0.2	0.3 ; 17.1 ± 0.2	0.3 ; 17.1 ± 0.2	
	100	54.2 ; 14.9 ± 7.5	57.8 ; 14.4 ± 7.5	48.2 ; 8.9 ± 8.2	48.3 ; 5.8 ± 3.3	5.41 ; 5.4 ± 3.4	20.9 ; 2.4 ± 4.2	9.5 ; 1.4 ± 0.4	7.8 ; 1.2 ± 0.5	1.8 ; 0.8 ± 0.5	
	353	47.8 ; 84.1 ± 48.4	52.9 ; 82.6 ± 48.3	41.7 ; 65.0 ± 47.2	5.6 ; 34.3 ± 6.2	5.6 ; 32.4 ± 6.2	5.5 ; 12.9 ± 6.5	0.7 ; 34.3 ± 0.8	0.7 ; 32.3 ± 0.8	0.7 ; 12.4 ± 0.8	

Table 2.6: Errors in polarization angle (in degrees) and intensity (in μK/arcmin), and the bias, ordered like $\sigma_\phi^{E,B}(90^\circ)$; $b_P \pm \sigma_P^{E,B}(90^\circ)$, characterizing the performance of the filter in each of the different scenarios considered. Note that, since the background emission and the instrumental noise are the main reason hindering the detection of the point-like sources, similar values of $\sigma_P^{E,B}(90^\circ)$ were obtained for every region and noise level. Highlighted cells, in blue for the E-mode, and in pink for the B-mode, show where detections where made. As a general rule, for the same regions, better results where obtained when working in B-mode maps.

CHAPTER 3

Mapping mass distribution in Galaxy Clusters

3.1 Data description

The *Gravitational Lensing Group* at Brown University is currently working on a project that aims to map the mass distribution of the largest sample of galaxy clusters to date. By the end of the project, around 400 clusters from the nearby universe, with redshifts between $z \in [0.03, 0.12]$, will be studied, and in those cases where images from different filters are available, estimates of the cluster's mass will also be obtained.

To reach this goal, images from the public data archives of the Arizona, Chile and Hawaii large telescopes are being pursued. These telescopes, combined with stacking techniques, allow the wide fields and long exposures needed to cover the whole galaxy cluster under study, and detect as many of the fainter background galaxies as possible. The Dark Energy Camera (DECam), mounted in the Blanco Telescope at the Cerro Tololo Inter-American Observatory (CTIO), is the preferred one due to its 2.2 degree field, which translates into approximately a 2 Mpc squared image for the redshifts of interest, ensuring the coverage of the whole cluster. In fact, the $z = 0.03$ lower limit of the sample is fixed as the distance to the nearest galaxy clusters that still fit in the DECam field, whereas the $z = 0.12$ upper limit is set for being the maximum redshift at which X-ray galaxy cluster catalogs are guaranteed to be complete (notice that, as mentioned in the introduction, X-ray radiation is a key element in the analysis of baryonic and dark matters in cluster's studies). The DECam focal plane consists of a hexagonal array of sixty-two 20488×4096 science CCDs specifically designed to measure the redshifted light from distant galaxies and stars for the Dark Energy Survey project [27].

When DECam images are not available, images from the Canada-France-Hawaii Telescope (CFHT) and the Subaru Telescope, both atop Mauna Kea in Hawaii, are used. The MegaCam at CFHT has a mosaic of thirty-six 2048×4612 pixel CCDs that covers a 1 square degree field [7] while the Subaru Prime Focus Camera (Suprime-Cam) counts with a mosaic of only ten 2048×4096 CCD, limiting its field to a 34'×27' region [26]. The Suprime-Cam is known for producing very sharp deep images due to the advanced system of adaptative optics that it mounts, allowing for better determination of the shape of the distant background galaxies. With less priority, images taken by the Hyper Suprime-Cam and MOSAIC I

and II cameras will also be analyzed.

For each cluster, images of different filters are necessary to obtain distance estimates of the galaxies, and also as a consistency check on the shear pattern. Information about the distances to the galaxies within the cluster and of the background, is fundamental to derive measurements of the cluster's mass from the projected mass density distributions. All filters present on the archives will be used, although few hopes are held in the ones that peak near the ultraviolet range due to the long exposure times required to capture the scarce ultraviolet light emitted by galaxy clusters. As previously discussed, X-ray data from the Chandra archive will be used to compare the spatial distribution of the cluster X-ray emission with the found mass distribution, drawing relations between the distribution of ordinary and dark matter.

For this work, images of the A2142 Abell Cluster taken with the CFHT's MegaCam were analyzed. A2142 was chosen for being the galaxy cluster with brightest X-ray emission in the selected volume according to HEARSARC's *Meta-Catalog of the compiled properties of X-ray detected Clusters of galaxies* (MCXC), suggesting that it will also possess a great mass. The images of A2142 in the G and R bands used to construct the galaxies catalog were selected amongst the stacked and PSF corrected images, already available at the Canada-France-Hawaii Telescope Legacy Survey archive (CFHTLS), for having long exposure times (1920 and 1320 seconds, respectively).

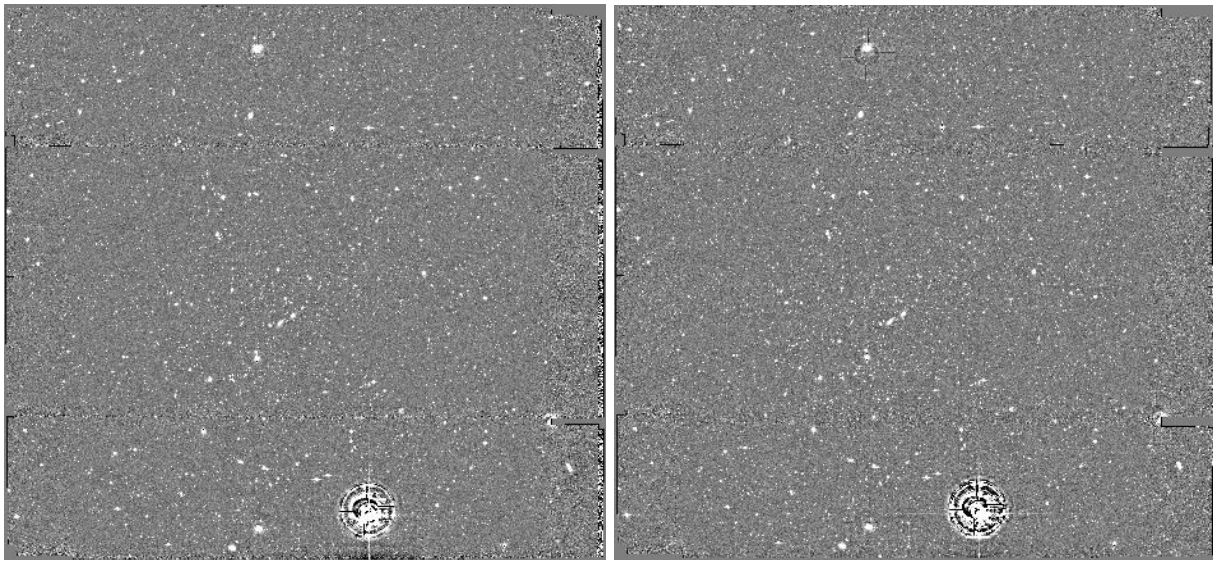

Figure 3.1: Images of the G (left) and R (right) band of A2142 taken by CFHT's MegaCam. With close inspection, A2142 can be found at the center of the image.

3.2 Catalog construction

The code used for the construction of the catalog is the *obs_file* wrapper of the *processCcd* code designed by the Large Synoptic Survey Telescope (LSST) Data Management team [4]. This code produces as it main outputs, a calibrated image (i.e., background subtracted, PSF corrected and cosmic rays and other defects removed) and a catalog of compact sources. Although the code was originally written to be the

first step in the process for measuring and combining individual exposures into a stack, here it was used on already treated images in order to obtain the catalog of compact objects with PSF corrected shapes, and their estimated fluxes.

From now on, the first object catalog produced by *obs_file* will be referred to as the *raw catalog*, and the final catalog that we derive (see below), as the *galaxy catalog*. The *raw catalog* contains every detected object, both stars and galaxies, and also some cosmic rays, star trails and image defects that must be filtered out to obtain the final *galaxy catalog*. Here the term *star trail* is coined to synthesize all kind of saturation effects distorting the brightness distribution of the image in the vicinity of the stars. Most of the filtering process is done by looking at the *magnitude vs size* graph (*mag vs size* graph for short). From this graph, it is possible to asses the atmospheric blurring effect and the accuracy of the stacking and PSF correction process. The *size* used in the *mag vs size* graph is computed as the sum of quadrupole moments $I_{xx} + I_{yy}$. This measurement of size keeps a quadratic relation with the object's size in number of pixels, so a small increase on the actual size of the object can appear quite drastic in the graph. Since we only plan to use the *mag vs size* graph to classify objects according to their sizes and brightnesses relative to one another, in the following plots the zero-level was arbitrarily chosen as the magnitude zero-point value, making use of the real fluxes of the objects when applying any filtering restriction to the *raw catalogs*.

As presented in the top panels of figure 3.2, one of the main features of the *mag vs size* graph is the horizontal line of small objects with roughly the same size but having a wide range of magnitude values (seen in yellow): this is the trace left by stars on the *mag vs size* graph. These highlighted objects are the ones *obs_file* recognized as stars and are used for the PSF correction. These star candidates are uniformly distributed over the whole image, ensuring a good PSF fit in all regions. Obviously, a spatially uniform distribution of the stars with which to calculate the PSF fit becomes highly important in images stacked from exposures with different atmospheric conditions, where the blurring of the image varies from region to region. When this happens, the *mag vs size* graph usually shows a broad stellar locus, or even two distinct ones. The upper limit size and the width of the stellar locus gives an idea of the blurring produced by the atmosphere, signaling that, in this case, we count with quite sharp images. The really bright objects peaking up at the brighter end (i.e., the left end) of the stellar locus correspond to extremely bright stars. When stars are bright enough to saturate the image, their light starts to bleed out into nearby pixels, resulting in the dramatic increase seen on their measured size.

Distant bright stars constitute the smallest actual sources detected in the *raw catalog* and mark the resolution limit of the image. Thus, objects detected with even smaller sizes will not have a trustworthy shape determination. Some of these objects are cosmic rays, since *processCcd* includes even single-pixel detections in the catalogs. As a general rule, the background galaxies in which we are interested, are larger than the stars contained in the stellar locus, and in no case have enough superficial brightness to saturate the image. In such manner, the first constraint imposed upon the *raw catalog* would only keep in the catalog objects larger than the biggest stars in the stellar locus and fainter than the saturated stars at the end of it. The objects excluded from the catalog with this cut are the ones represented in red in figure 3.2. Since the stars selected by *processCcd* to compute its PSF model make for an arguably conservative stellar locus, magnitude and size limits are manually chosen for this cut as displayed in table 3.2.

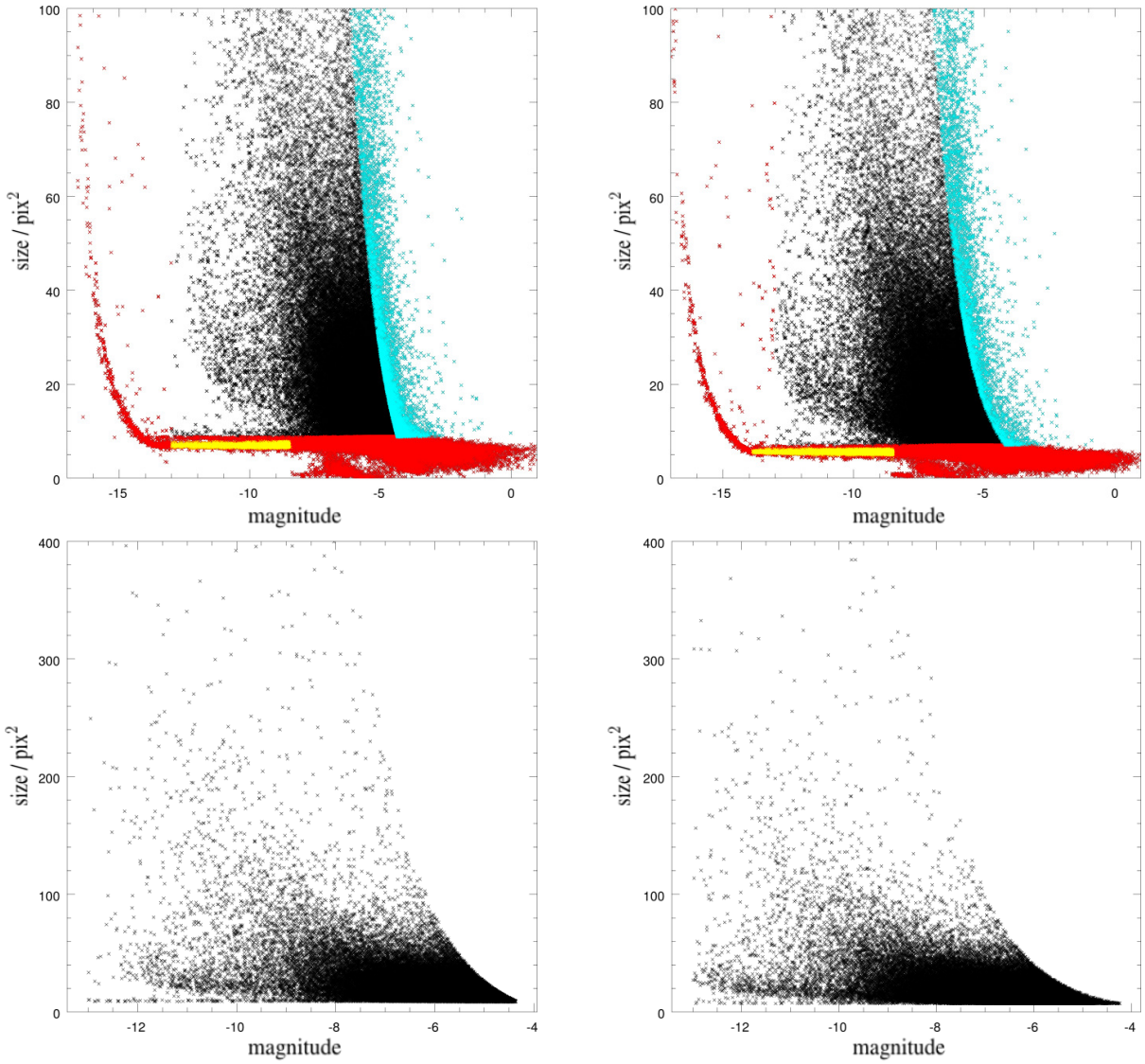

Figure 3.2: Images on the left correspond to the G band, and images on the right, to the R band. For this plots, the zero-level was arbitrarily chosen as the magnitude zero-point value. Top panel: *mag vs size* graph of the *raw catalogs*. The objects that *processCcd* recognised as stars (used to calculate the PSF model) are represented in yellow. Objects seen in red are the ones excluded for being smaller than the biggest stars in the stellar locus and having saturating fluxes. Since the stars selected by *processCcd* make for an arguably conservative stellar locus, broader magnitude and size limits were manually chosen for this cut, explaining why some of the objects in red are bigger than the stars in yellow. Blue objects are considered to be star trails, blob parents of the deblending process and faint detections that introduce more noise than signal to the map due to poor shape determination. Lower panel: *mag vs size* graph of the final *galaxy catalogs*. All the objects present satisfy the $e_+^2 + e_\times^2 < 4$ condition and have passed the visual inspection.

Objects near the logarithmic slope at the faint end of the *mag vs size* graph, the ones highlighted in blue in figure 3.2, are also excluded from the *galaxy catalog*. The *processCcd* detection procedure firstly identifies regions concentrating high superficial brightness, usually as a result of being affected by several sources, and secondly starts the *deblending* process of disentangling the light coming from each source to reconstruct them as individual objects. Both, the *parent* undefined blobs and the separate *children* objects, are included in the *raw catalog*. The bulk of the largest objects in blue is made from these parent blobs and from some very elongated star trails that *processCcd* recognises as independent objects. In turn, the medium to small size blue objects are excluded because, although the majority of them are valid detections (easily a 4σ above the background in most cases), the received number of photons is too low to

amount to a good shape determination. If they lie near another bright object, the added light also distorts the shape estimation. All in all, these objects introduce more noise than signal on the map, justifying their removal from the catalog. The constraint needed to exclude these objects from the catalog is logarithmic in the *magnitude vs size* domain, but becomes linear if we work instead in the *flux vs size* domain (second restrictions in table 3.1).

Not a negligible number of the objects surviving the previous cuts present ellipticities e_+ and $e_\times$ values greater than one. This is a consequence of how the algorithms in *processCcd* attempt to reconstruct the ellipticity galaxies would have had *before* atmospheric blurring and telescope distortion. To counteract some of the worst effects of this shape correction method without losing to many galaxies, the detected objects with ellipticity components greater than two are removed from the catalog. This constraint is implemented requiring objects to fulfill the $e_+^2 + e_\times^2 < 4$ condition (third restriction in table 3.1). Some of the remainig elongated star trails *processCcd* identified as compact objects are also filtered out with this restriction. After this cut, only 15% of the remaining objects have ellipticities greater than one.

In the last step of the catalog construction, the estimated shapes of the detected object are overlaid onto the initial image, proceeding to painstakingly manually remove the non-galaxy objects. The main objective is to remove the star trails and deblending parent blobs that passed the previous cuts and objects of dubious detection, or whose shape was clearly badly determined. Critical regions in which to look for these objects are those around large bright stars and CCD edges. Very bright stars tend to have a lot of spurious detections in their outskirts, often in a ring-like pattern that can create a non-negligible lensing signal due to the tangential nature of their estimated shapes. In the vicinity of CCD edges, some objects get partially cut out of the image or barely stand over the slightly brigther background, making their detected shapes not trustworthy. The complete lack of information at the outer side of external edges increases the weight these objects have on the calculation of the projected mass map, resulting in noisier edge regions. Maintaining the aforementioned objects in the final catalog could create a systematic error signal. Since the lensing signal at each point is computed taking into account all the objects inside an extended ring, the gaps between internal CCD edges do not suppose a major problem.

Catalog	Restriction imposed	initial objects	objects after cut
raw catalog G band	$I_{xx} + I_{yy}$ >8.8 & mag> -13 (i.e. flux< 158489)	200796	102333
	$I_{xx} + I_{yy}$ < -12.18+0.3818×flux	102333	91376
	e_+^2+$e_\times^2$ <4	91376	73718
galaxy catalog G band	visual inspection	73718	71886
raw catalog R band	$I_{xx} + I_{yy}$ >7 & mag> -13 (i.e. flux< 158489)	206932	106052
	$I_{xx} + I_{yy}$ < -0.768+0.1623×flux	106052	96923
	e_+^2+$e_\times^2$ <4	96923	77378
galaxy catalog R band	visual inspection	77378	73762

Table 3.1: Filtering conditions imposed onto the *raw catalogs* produced by *obs_file* in order to produce the final *galaxy catalogs*. For each filtering step, the effect of the imposed constraints can be appreciated in the number of objects present before and after the cut. While filtering conditions are applied to the catalogs in terms of flux, the first constraints applied are also shown in terms of magnitude to allow their understanding in the context of the previously displayed *mag vs size* graphs.

The *mag vs size* graphs containing the objects that made it into the final *galaxy catalog* are shown in

the lower panel of figure 3.2. A quick and simple estimation based on the final number of galaxies in each catalog, foretells that a decent signal-to-noise ratio will be possible for the projected mass density maps. For the lensing signal produced by the average mass cluster to surpass the nondescript signal a random orientation of galaxies creates, and reach a signal-to-noise ratio of $S/N \sim 1$, at least around ~ 20000 galaxies should be inside the influence area described between the r_{in} and r_{out} radii of the weight function in equation (3.3). Using the values $r_{in} = 1000$ pix and $r_{out} = 10000$ pix as radii, this implies a galaxy density of $\mathrm{density}_{\mathrm{gal}} = \#\mathrm{galaxies}/2\pi(r_{out}^2 - r_{in}^2) \approx 3.22 \times 10^{-5}$ galaxies/pix. Extending this density to the whole 22676×20871 image of the CFHT's MegaCam ($\mathrm{Area}_{\mathrm{image}} = 22676 \times 20871 \approx 4.73 \times 10^8$ pix^2), then around $\mathrm{density}_{\mathrm{gal}} \times \mathrm{Area}_{\mathrm{image}} \approx 15000$ galaxies are needed to amount to a $S/N \sim 1$. Since lensing signal increases like the square root of the number of galaxies, and we have almost five times that number of objects in the *galaxy catalogs*, a signal-to-noise ratio of around $S/N \sim 2.2$ may be expected.

3.3 Maps of projected mass density

The projected mass density map is computed from the positions and ellipticities of the objects in the *galaxy catalog*. As sketched in figure 3.3, for every given point (x, y), the ellipticity components of every object are recalculated respectively to it. The new tangential (e_t) and cross (e_c) ellipticities are easily computed from the e_+ and $e_\times$ values collected in the catalog like [31]:

$$\begin{aligned} e_t &= e_+ \cos 2\theta + e_\times \sin 2\theta, \\ e_c &= -e_+ \sin 2\theta + e_\times \cos 2\theta, \end{aligned} \tag{3.1}$$

where θ is the polar angle specifying the $\vec{r}_i = (r_i, \theta_i)$ position of each galaxy's centroid with respect to the considered point (x, y).

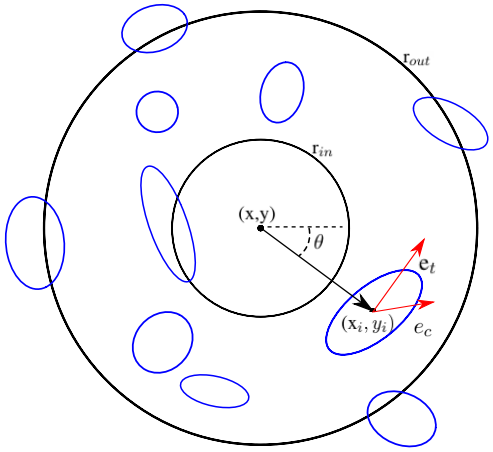

Figure 3.3: For each (x, y) point, the projected mass density is computed as the sum of the tangential ellipticity e_t over the square distance to all objects in the catalog. Due to the applied weighting function, only objects inside the ring defined by r_{in} and r_{out} have a significant effect.

The projected mass density at each point is then computed like:

$$\kappa(\vec{r}) = \frac{1}{\sum \omega(|\vec{r}|)} \sum_i^N \frac{e_t^i \omega(|\vec{r} - \vec{r}_i|)}{|\vec{r} - \vec{r}_i|^2}, \tag{3.2}$$

using the $\omega(r)$ function

$$\omega(r) = e^{-r/r_{out}}(1 - e^{-r/r_{in}}) \tag{3.3}$$

to deweight the effects of distant and nearby objects [13]. As displayed in figure 3.3, the r_{in} and r_{out} parameters define a ring-like region of influence, making negligible the effects of too close or too distant galaxies. The value of r_{in} also plays a role to define the resolution and signal-to-noise ratio of the final map. A small value of r_{in} results in sharper contours that increase the resolution of the map, allowing for a better determination of substructure, at the price of a lower S/N ratio. A higher value of r_{in} has a smoothing effect over the map, perhaps rendering differentiated features into unsolvable lumps, but increasing the signal-to-noise ratio.

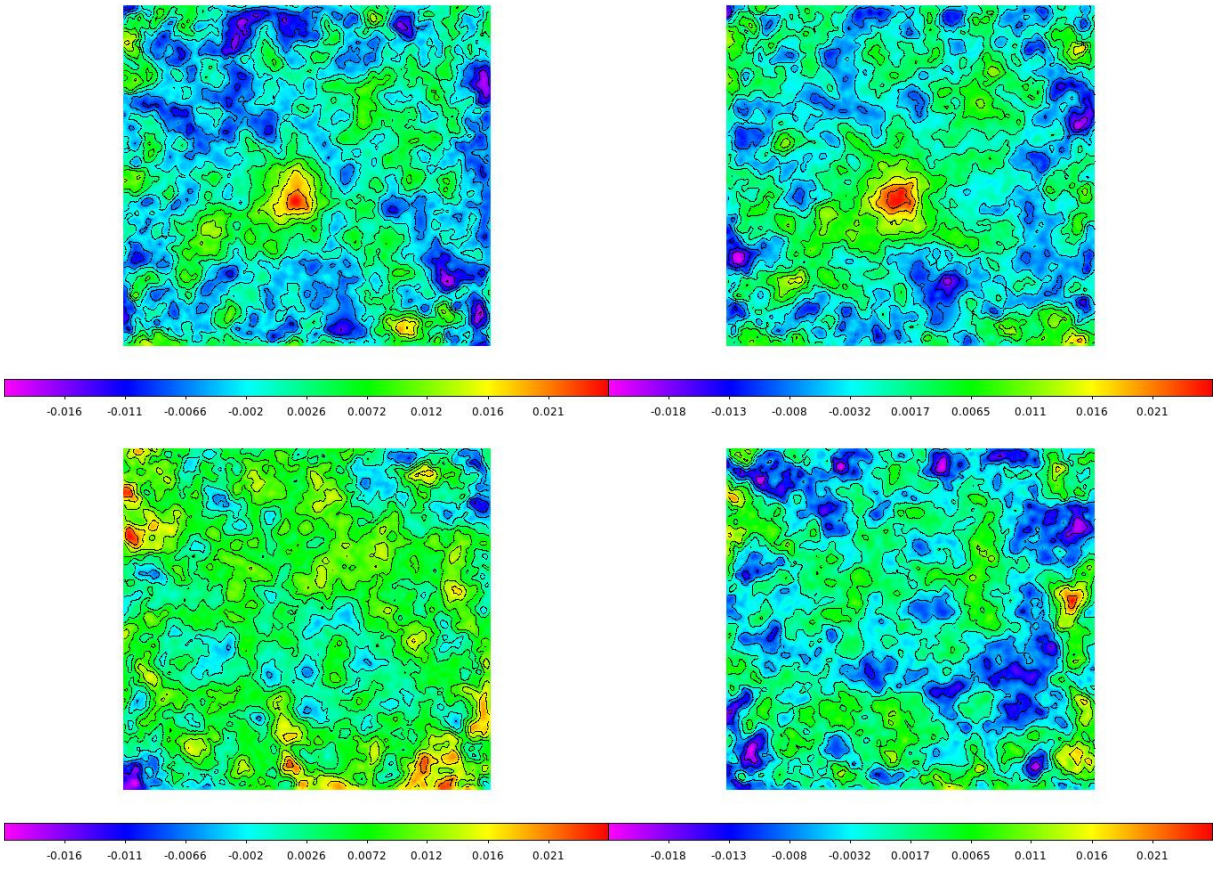

Figure 3.4: Images on the left correspond to the G band, and images on the right, to the R band. Top panel: Contour maps of the projected mass density computed from the *galaxy catalog*. Lower panel: 45° test maps that act as an estimation of the B-mode, i.e, indicating noisy regions and systematic errors.

Rotating every object 45°, which can be done by swapping e_t for e_c in equation (3.2), we get a noise estimation map known as the *45° test*. In this test, the lensing signal should disappear, therefore non-zero results reflect noisier regions or systematic errors. This test is based on the curl-free nature (to first order) of the shear field produced by lensing. Intrinsic alignments in the shape of galaxies, like the ones produced by cosmic shear, a bad PSF correction, and basically any non-lensing signal, result in a curl shear field. As happened with the CMB, this curl-free and divergence-free fields are called E- and B-modes. The 45° test is useful for being a crude estimation of this B-mode field.

The projected mass density maps obtained from the *galaxy catalogs*, and their respective 45° test maps, are shown in figure 3.4. Overlaying the contour maps with the original optical image, as can be seen in figure 3.5, it is verified that the clear maximums present in the G and R band maps lie where the cluster is expected to be, by looking at the galaxies distribution in the optical image. G and R band maps of projected mass distribution also point to overdensities in the upper right region, top left and lower right corners of the image. On the other hand, B-mode maps of the G and R band do not present any clear correlation, denoting no alarming systematic errors.

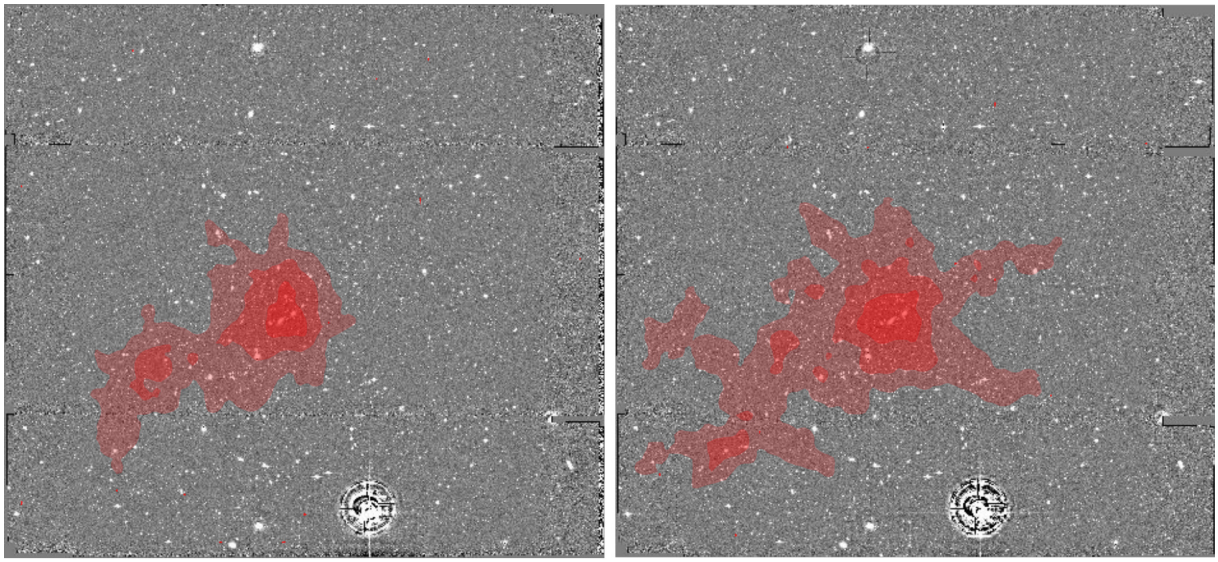

Figure 3.5: Contour maps of projected mass density computed from the *galaxy catalog* overlaid onto the G band (left) and R band (right) optical images. As expected, the maximum density peak surrounds A2142.

With these maps, we obtain two detections of the A2142 cluster at a 3.2σ significance in the G band map, and at 2.9σ for the R band map. These detections cannot be considered independent since G and R optical images contain almost the same information regarding the shape of the detected galaxies. For the detections to be considered independent, a more complex and detailed analysis extricating the light coming from each galaxy in G and R filters and the slightly different galaxies shapes obtained from them would be needed. No other clear substructure stands out above the 2.5σ threshold.

CHAPTER 4

Conclusions and future work

Point-like source detection in polarization maps of the Cosmic Microwave Background

The application of the filter to the different simulated scenarios shows that it will be possible to detect point-like sources with a minimum flux of 1Jy (assuming a polarization degree of 30%) in the E- and B-mode polarization maps coming from future missions like LiteBIRD (with sensitivities corresponding to the simulated noise level $\sigma_{n,3}$). Based on the smaller biases and errors in the determination of polarization angle and intensity obtained when working with the B-mode map rather than with the E-mode map of the same region, it can also be affirmed that operating on B-mode maps is definitely beneficial for the detection and characterization of point-like sources. Since the main reason making B-mode maps a better place to look for point-like sources than E-mode maps, is the lower amplitude of the CMB B-modes, it is also derived that working with B-mode polarization maps will also report better results than the conventional approach of directly detecting point-like sources on the Stokes' parameters Q and U maps.

Since the filter performance was characterized for only one filter scale (indeed, the scale of the PSF was taken), this aspect of the wavelet nature remains unexplored. As it can be done for other wavelet-based filters, exploring the different filter scales and finding the one that maximizes the amplification of the wavelet coefficients, will improve the overall filter performance. Hopefully, the filter scale maximizing amplification will also minimize the errors committed in polarization angle and intensity. With this optimum filter scale, biases could be reduced, potentially extending the possibility of detecting point-like sources to regions of the sky with stronger foreground emission to fainter sources. This will be a point of future study.

Although the application here explored was limited to sources of known position, the extension to *blind detection* applications will also be very interesting. The conventional techniques used for the detection of point-like sources, tend to fix a detection threshold in intensity, that results in a detection threshold in polarization. This strategy favors the detection of the point-like sources that keep a certain relation between polarization and intensity (i.e., a certain polarization degree). Some sources dismissed for not clearing the detection threshold in intensity, potentially may have a polarization degree larger than average, that would raise them above the detection threshold in polarization. As a result, the produced catalog of detected sources is potentially biased, ruining the analysis of the polarization physics of point-like sources.

The designed filter already proved that operating in B-mode maps is beneficial with respect to these usual approaches, and may help to produce blind catalogs, directly in polarization, free of these biases.

Estimation of Dark Matter distribution in galaxy clusters

The maps of projected mass density of the A2142 Abell galaxy cluster included in this work, are just an example of the kind of maps the *Gravitational Lensing Group* at Brown University is currently constructing in the first stages of their new project. With the use of the sharper and deeper images from the DECam, they will be able to produce maps of projected mass density of higher resolution and signal-to-noise ratios. Their goal is to map the 400 galaxy clusters in the nearby universe with the brightess X-ray emission.

In future steps, distance estimates for the galaxies within the clusters will be obtained applying photometric redshift techniques to the images of the clusters coming from different filters. This information will make possible the transformation of projected mass density into actual measurements of mass.

The combination of the projected mass density maps produced in the project, with the distribution of galaxies coming from optical images, and the information of where the majority of baryonic mass is located infered by images of X-ray emission, will help to further constrain the properties of dark matter, especially its capability of self-interaction.

Bibliography

[1] Abramowitz, M. and Stegun, I. A. (1964) *Handbook of Mathematical Functions with Formulas, Graphs, and Mathematical Tables*. Ninth printing. Dover Publications pp. 486,505. ISBN-10: 0486612724

[2] Baddour, N. (2011) Two-Dimensional Fourier Transforms in Polar Coordinates. *Advances in Imaging and Electron Physics* **165** pp. 1-45 doi: 10.1016/B978-0-12-385861-0.00001-4

[3] Baumann, D. (2009) TASI Lectures on Inflation. *arXiv astrophysics e-prints* arXiv:0907.5424v2[hep-th]

[4] Bosch, J., Armstrong, R., Bickerton, S., et al. (2018) The Hyper Suprime-Cam Software Pipeline. *Publications of the Astronomical Society of Japan* **70**(SP1), S5(1-40) doi:10.1093/pasj/psx080

[5] Boyarsky, A., Ruchayskiy, O. and Shaposhnikov, M. (2009) The Role of Sterile Neutrinos in Cosmology and Astrophysics (2009). *Annual Review of Nuclear and Particle Science* **59** pp.191-214. doi:10.1146/annurev.nucl.010909.083654

[6] Cabella, P. and Kamionkowski, M. (2004) Theory of Cosmic Microwave Background Polarization. *arXiv astrophysics e-prints* arXiv:astro-ph/0403392v2

[7] Canada-France-Hawaii-Telescope. *MegaPrime/MegaCam*. Accessed:8/15/2018. http://www.cfht.hawaii.edu/Instruments/Imaging/Megacam/index.html

[8] Carr, B., Kühnel, F. and Sandstad, M. (2016) Primordial Black Holes as Dark Matter. *Physical Review D*, **94**8. doi:10.1103/PhysRevD.94.083504

[9] CMB-S4 Colaboration, Abazajian, K. N., Adshead, P., et al. (2016) CMB-S4 Science Book, First Edition. *arXiv astrophysics e-prints* p. 17 arXiv:1610.02743v1 [astro-ph.CO]

[10] Courbin, F., Saha, P. and Schechter, P. L. (2002) Quasar Lensing in *Gravitational Lensing: An Astrophysical Tool (Lecture Notes in Physics)* Courbin, F. and Minniti, D. (Eds). Springer-Verlag Berlin. ISBN:3-540-44355-X

[11] Dickinson, C. (2016) CMB foregrounds - A brief overview. *arXiv astrophysics e-prints* arXiv:1606.03606 [astro-ph.CO]

[12] Drees, M. and Gerbier, G. (2012) Mini-Review of Dark Matter: 2012. *arXiv astrophysics e-prints* arXiv:1204.2373 [hep-ph]

[13] Fischer, P. and Tyson, J. A. (1997) The Mass Distribution of the most Luminous X-ray Cluster RXJ 1347.5-1145 from Gravitational Lensing *The Astronomical Journal* **114**1 pp.14-24 doi:10.1086/118447

[14] Freeman, W. T. and Adelson, E. H. (1991) The Design and Use of Steerable Filters. *IEEE Transactions on Pattern Analysis and Machine Intelligence* **13**(9) pp. 891-906.

[15] Frieman, J. (2008) Lectures on Dark Energy and Cosmic Acceleration. *American Institute of Physics Conference Series* **1057** pp. 87-124. doi:10.1063/1.3000000

[16] Garrett, K. and Gintaras, D. (2011) Dark Matter: A Primer. *Advances in Astronomy* [968283]. doi: 10.1155/2011/968283

[17] Gorski, K., Wandelt, B., Hansen, F., Hivon, E., and Banday, A. (1999) *The HEALPix primer*. Version 3.40. Available at:https://healpix.sourceforge.io/documentation.php

[18] Hobson, M. P., Jones, A. W., Lasenby, A. N. and Bouchet, F. R. (1998) Foreground separation methods for satellite observations of the cosmic microwave background. *Monthly Notices of the Royal Astronomical Society* **300**1, pp. 1-29. doi: 10.1046/j.1365-8711.1998.01777.x

[19] Kahlhoefer, F., Schmidt-Hoberg, K., Frandsen, M. T. and Sarkar, S. (2014) Colliding clusters and dark matter self-interactions. *Monthly Notices of the Royal Astronomical Society* **437**3, pp.2865-2881. doi:10.1093/mnras/stt2097

[20] Kamionkowski, M., Kosowsky, A. and Stebbins, A. (1997) A Probe of Primordial Gravity Waves and Vorticity *Physical Review Letters* **78**(11) pp. 2058-2061. doi: 10.1103/PhysRevLett.78.2058

[21] Peccei, R. D. (2008) The Strong CP Problem and Axions in *Axions (Lecture Notes in Physics)*. Volume 741. Springer-Verlag Berlin. ISBN:978-3-540-73517-5. Heidelberg, 2008, p. 3

[22] Planck Collaboration, Adam, R., Ade, P. A. R., et al. (2016) Planck 2015 results. Overview of products and scientific results. *Astronomy & Astrophysics* **594**, A1(2016) doi: 10.1051/0004-6361/201527101

[23] Planck Collaboration, Ade, P. A. R, Aghanim, N., et al. (2016) Planck 2015 results. XXVI. The Second Planck catalogue of Compact Sources. *Astronomy & Astrophysics* **594**, A26(2016) doi:10.1051/0004-6361/201526914

[24] Roszkowski, L., Sessolo, E. M, and Trojanowski, S. (2018) WIMP dark matter candidates and searches—current status and future prospects. *Reports on Progress in Physics* **81**6. doi:10.1088/1361-6633/aab913

[25] Samtleben, D., Staggs, S. and Winstein, B. (2008) The Cosmic Microwave Background for Pedestrians: A Review for Particle and Nuclear Physicists. *Annual Review of Nuclear and Particle Science* **57**(1) doi:10.1146/annurev.nucl.54.070103.181232

[26] Subaru Telescope. *Suprime-Cam*. Accessed: 8/15/2018. https://subarutelescope.org/Observing/Instruments/SCam/index.html

[27] The Dark Energy Survey. *The Camera*. Accessed:8/15/2018. https://www.darkenergysurvey.org/the-des-project/instrument/the-camera/

[28] Thorne, B., Dunkley, J., Alonso, D. and Naess, S. (2017) The Python Sky Model: software for simulating the Galactic microwave sky. *Monthly Notices of the Royal Astronomical Society* **469**(3) pp. 2821–2833 doi:10.1093/mnras/stx949

[29] Tulin, S. and Yu, H. (2018) Dark matter self-interactions and small scale structure. *Physics Reports* **730**, pp. 1-57. doi:10.1016/j.physrep.2017.11.004

[30] Wiaux, Y., Jacques, L. and Vandergheynst, P. (2005) Correspondence Principle between Spherical and Euclidean Wavelets *The Astrophysical Journal* **632**(1) pp. 15-28. Retrievable at: http://iopscience.iop.org/article/10.1086/432926

[31] Wittman, D. (2002) Weak lensing in *Gravitational Lensing: An Astrophysical Tool (Lecture Notes in Physics)* Courbin, F. and Minniti, D. (Eds). Springer-Verlag Berlin. ISBN:3-540-44355-X.

APPENDIX **A**

Deduction of point-like source profile in real space E-modes

A step-by-step transformation of the source E-mode profile from the Fourier to the real space will be adressed. Since the process is analogous for E- and B-modes, only the E-mode case will be presented. To simplify operations, we start by rewriting the $\tilde{P}_E$ profile displayed in equation (2.4) as:

$$\tilde{P}_E(\vec{q}) = \frac{1}{2}[Q\cos 2\theta + U\sin 2\theta]\tilde{\rho}(q), \tag{A.1}$$

where polarization information is condensed in Q and U Stokes' parameters defined like:

$$Q = P\cos 2\phi, \qquad U = P\sin 2\phi, \tag{A.2}$$

and the radial profile is:

$$\tilde{\rho}(q) = \frac{\sigma^2}{2\pi}e^{-q^2\sigma^2/2}. \tag{A.3}$$

For non-radially symmetric functions like this one, the inverse Fourier transform in polar coordinates $\vec{q} = (q, \theta)$ can be calculated expanding the function into its Fourier series [2] like:

$$f(r,\xi) = \sum_{n=-\infty}^{\infty} \frac{1}{2\pi} i^n e^{in\xi} \int_0^\infty \tilde{f}_n(q) J_n(qr) q dq, \tag{A.4}$$

where $J_n(x)$ is the n-order Bessel function, and the Fourier coefficients $\tilde{f}_n(q)$ are given by:

$$\tilde{f}_n(q) = \frac{1}{2\pi}\int_0^{2\pi} \tilde{f}(q,\theta)e^{-in\theta}d\theta. \tag{A.5}$$

According to these equations, the first step would be to calculate the Fourier coefficients $\tilde{P}_{En}(q)$ of the source's profile:

$$\begin{aligned}\tilde{P}_{En}(q) &= \frac{1}{2\pi}\int_0^{2\pi}\tilde{P}_E(q,\theta)e^{-in\theta}d\theta = \frac{\tilde{\rho}(q)}{4\pi}\int_0^{2\pi}[Q\cos 2\theta + U\sin 2\theta]e^{-in\theta}d\theta = \\ &= \frac{\tilde{\rho}(q)}{4\pi}\int_{-\pi}^{\pi}\Big[Q\cos 2\theta(\cos n\theta - i\sin n\theta) + U\sin 2\theta(\cos n\theta - i\sin n\theta)\Big]d\theta.\end{aligned} \tag{A.6}$$

Since we are integrating in a periodic interval, the terms $\cos 2\theta \sin n\theta$ and $\sin 2\theta \cos n\theta$ cancel out due to parity, leaving us with:

$$\tilde{P}_{En}(q) = \frac{\tilde{\rho}(q)}{4\pi}\int_{-\pi}^{\pi}\Big[Q\cos 2\theta\cos n\theta - iU\sin 2\theta\sin n\theta\Big]d\theta. \tag{A.7}$$

We must now distinguish between the $n \neq \pm 2$ and $n = \pm 2$ cases to solve this integral. The $n \neq \pm 2$ terms cancel out, since:

$$\begin{aligned}\tilde{P}_{E\neq 2}(q) &= \frac{\tilde{\rho}(q)}{4\pi}\int_{-\pi}^{\pi}\frac{1}{2}\Big[(Q-iU)\cos(2-n)\theta + (Q+iU)\cos(2+n)\theta\Big]d\theta = \\ &= \frac{\tilde{\rho}(q)}{8\pi}\Big|(Q-iU)\frac{\sin(2-n)\theta}{2-n} + (Q+iU)\frac{\sin(2+n)\theta}{2+n}\Big|_{-\pi}^{\pi} = 0,\end{aligned} \tag{A.8}$$

leaving us only with the non-null $n = \pm 2$ terms:

$$\begin{aligned}\tilde{P}_{E\pm 2}(q) &= \frac{\tilde{\rho}(q)}{4\pi}\int_{-\pi}^{\pi}\Big[Q\cos^2 2\theta \mp iU\sin^2 2\theta\Big]d\theta = \\ &= \frac{\tilde{\rho}(q)}{8\pi}\int_{-\pi}^{\pi}\Big[(Q\mp iU) + (Q\pm iU)\cos 4\theta\Big]d\theta = \frac{\tilde{\rho}(q)}{4}(Q\mp iU),\end{aligned} \tag{A.9}$$

as one may have predicted just by looking at the $\cos 2\theta$, $\sin 2\theta$ angular dependence of $\tilde{P}_E(\vec{q})$. Therefore, the Fourier series expansion is limited to the $n = \pm 2$ terms:

$$P_E(r,\xi) = -\frac{1}{2\pi}\Big(e^{i2\xi}\int_0^{\infty}\tilde{P}_{E2}(q)J_2(qr)qdq + e^{-i2\xi}\int_0^{\infty}\tilde{P}_{E-2}(q)J_{-2}(qr)qdq\Big), \tag{A.10}$$

and, due to the $J_{-n}(x) = (-1)^n J_n(x)$ property of Bessel functions, $J_{-2}(qr) = J_2(qr)$, it finally reads:

$$\begin{aligned}P_E(r,\xi) &= -\frac{1}{8\pi}\Big(e^{i2\xi}(Q-iU) + e^{-i2\xi}(Q+iU)\Big)\int_0^{\infty}\tilde{\rho}(q)J_2(qr)qdq = \\ &= -\frac{1}{4\pi}\Big(Q\cos 2\xi + U\sin 2\xi\Big)\int_0^{\infty}\tilde{\rho}(q)J_2(qr)qdq.\end{aligned} \tag{A.11}$$

To solve the radial integral of the profile,

$$\int_0^{\infty}\tilde{\rho}(q)J_2(qr)qdq = \frac{\sigma^2}{2\pi}\int_0^{\infty}e^{-q^2\sigma^2/2}J_2(qr)qdq, \tag{A.12}$$

we use the tabulated [1] formulas of the known integrals of Bessel functions:

$$\int_0^{\infty}e^{-a^2t^2}t^{\mu-1}J_\nu(bt)dt = \frac{\Gamma\Big(\frac{1}{2}\nu+\frac{1}{2}\mu\Big)\Big(\frac{b}{2a}\Big)^\nu}{2a^\mu\Gamma(\nu+1)}M\Big(\frac{1}{2}\nu+\frac{1}{2}\mu,\nu+1,-\frac{b^2}{4a^2}\Big), \tag{A.13}$$

where the $M(a,b,z)$ confluent hypergeometric function is:

$$M(a,b,z) = \frac{\Gamma(b)}{\Gamma(a)\Gamma(b-a)}\int_0^1 e^{zu}u^{a-1}(1-u)^{b-a-1}du. \tag{A.14}$$

Parameter identification comparing equations (A.13) and (A.12) leads us to:

$$\frac{\sigma^2}{2\pi}\int_0^{\infty}e^{-q^2\sigma^2/2}J_2(qr)qdq = \frac{1}{4\pi}\Big(\frac{r^2}{2\sigma^2}\Big)M\Big(2,3,-\frac{r^2}{2\sigma^2}\Big), \tag{A.15}$$

where the specific confluent hypergeometric function, in terms of a generic variable z, is

$$M(2,3,z) = \frac{\Gamma(3)}{\Gamma(2)\Gamma(1)}\int_0^1 e^{zu}udu = 2\int_0^1 e^{zu}udu. \tag{A.16}$$

To solve the integral above, we apply the $x = e^{zu}$ variable change. This way, the integral can be solved for the generic z variable like:

$$M(2,3,z) = 2\int_0^1 e^{zu}udu = 2\int_1^{e^z} x\frac{1}{z}lnx\frac{1}{zx}dx = \frac{2}{z^2}\int_1^{e^z} lnxdx = \\ = \frac{2}{z^2}\Big|xlnx - x\Big|_1^{e^z} = \frac{2}{z^2}\Big(1 + e^z(z-1)\Big). \tag{A.17}$$

With this result at hand, and substituting now the generic z varibale for $z = -r^2/2\sigma^2$, the radial term of the source's profile reads:

$$\frac{1}{4\pi}\Big(\frac{r^2}{2\sigma^2}\Big)M\Big(2,3,-\frac{r^2}{2\sigma^2}\Big) = \frac{1}{4\pi}\Big(\frac{r^2}{2\sigma^2}\Big)\frac{8\sigma^4}{r^4}\Big(1 - e^{-r^2/2\sigma^2}\Big(1 + \frac{r^2}{2\sigma^2}\Big)\Big) = \\ = \frac{\sigma^2}{\pi r^2}\Big(1 - e^{-r^2/2\sigma^2}\Big(1 + \frac{r^2}{2\sigma^2}\Big)\Big). \tag{A.18}$$

Joining radial and angular terms, the source profile adds up to the equation previously presented in (2.5) and (2.6):

$$P_E(r,\xi) = \frac{1}{4\pi^2}\Big(Q\cos 2\xi + U\sin 2\xi\Big)\frac{\sigma^2}{r^2}\Big(e^{-r^2/2\sigma^2}\Big(1 + \frac{r^2}{2\sigma^2}\Big) - 1\Big). \tag{A.19}$$

APPENDIX **B**

Deduction of the ω_x^E and ω_y^E wavelet coefficients

As in Appendix A, since the process is analagous for the source's profile in E- and B-modes, only the deduction of the wavelet coefficients ω_x^E and ω_y^E will be explicitly addressed. For the computation of these wavelet coefficients, we star by substituting the $\tilde{P}_E(q,\theta,\phi)$ profile in equations (2.19) like:

$$\begin{aligned}\omega_x^E(r,\xi,\phi,R) &= IFT\Big[\frac{1}{2}\Big(Q\cos^2 2\theta + U\cos 2\theta \sin 2\theta\Big)\mu(q,R)\Big],\\ \omega_y^E(r,\xi,\phi,R) &= IFT\Big[\frac{1}{2}\Big(Q\cos 2\theta \sin 2\theta + U\sin^2 2\theta\Big)\mu(q,R)\Big],\end{aligned} \tag{B.1}$$

where the polarization information is condensed in the Q and U terms (like previously defined in (A.2)), and $\mu(q,R)$ is the product of the radial terms of $\psi_{x,y}$ and $\tilde{P}_E$:

$$\mu(q,R) = \frac{\sigma^2 R^2}{4\pi^2} e^{-q^2(\sigma^2+R^2)/2}. \tag{B.2}$$

Note that while the profile of the source is fixed by the σ imposed by the PSF, we can play with the size of filter by changing its scale (R).

Expanding the $\sin^2 2\theta$, $\cos^2 2\theta$ and $\cos 2\theta \sin 2\theta$ terms, the previous equations can be divided into two different components:

$$\omega_x^E(r,\xi,\phi,R) = IFT\Big[\frac{Q}{4}\mu(q,R)\Big] + IFT\Big[\frac{1}{4}\Big(Q\cos 4\theta + U\sin 4\theta\Big)\mu(q,R)\Big], \tag{B.3}$$

$$\omega_y^E(r,\xi,\phi,R) = IFT\Big[\frac{U}{4}\mu(q,R)\Big] + IFT\Big[\frac{1}{4}\Big(Q\sin 4\theta - U\cos 4\theta\Big)\mu(q,R)\Big]. \tag{B.4}$$

For the first component, that only has a radial dependence, the inverse Fourier transform can be computed bearing in mind the relation:

$$\int_0^\infty e^{-\alpha z^2/2} e^{+iJz} dz = \Big(\frac{2\pi}{\alpha}\Big)^{1/2} e^{-J^2/2\alpha}. \tag{B.5}$$

Rewriting the radial componenet in Cartesian coordinates, the identificaton of (B.5) in it is immediate, and the inverse Fourier transform is then:

$$IFT\Big[\mu(q,R)\Big] = \frac{\sigma^2 R^2}{8\pi^3}\int_0^\infty e^{-(q_x^2+q_y^2)(\sigma^2+R^2)/2} e^{i(q_x x+q_y y)} dq_x dq_y = \frac{\sigma^2 R^2}{4\pi^2(\sigma^2+R^2)} e^{-r^2/2(\sigma^2+R^2)}. \tag{B.6}$$

For the second component, as it has both, radial and angular dependences, we must compute its inverse Fourier transform following equations (A.4) and (A.5). Starting with the ω_x^E wavelet coefficient, its $\tilde{\omega}_{xn}^E(q)$ Fourier coefficients are:

$$\begin{aligned}\tilde{\omega}_{xn}^E(q) &= \frac{1}{8\pi}\mu(q,R)\int_{-\pi}^{\pi}\Big(Q\cos 4\theta + U\sin 4\theta\Big)e^{-in\theta}d\theta = \\ &= \frac{1}{8\pi}\mu(q,R)\int_{-\pi}^{\pi}\Big[Q\cos 4\theta(\cos n\theta - i\sin n\theta) + U\sin 4\theta(\cos n\theta - i\sin n\theta)\Big]d\theta.\end{aligned} \tag{B.7}$$

Due to parity, the integral of odd terms $\cos 4\theta \sin n\theta$ and $\sin 4\theta \cos n\theta$ over an even interval cancels out, leaving us only with:

$$\tilde{\omega}_{xn}^E(q) = \frac{1}{8\pi}\mu(q,R)\int_{-\pi}^{\pi}\Big[Q\cos 4\theta\cos n\theta - iU\sin 4\theta\sin n\theta)\Big]d\theta. \tag{B.8}$$

Similarly as for $\tilde{P}_{En}(q)$, the $n \neq \pm 4$ terms are null, and the remaining $n = \pm 4$ terms read:

$$\begin{aligned}\tilde{\omega}_{x\pm 4}^E(q) &= \frac{1}{8\pi}\mu(q,R)\int_{-\pi}^{\pi}\Big[Q\cos^2 4\theta \mp iU\sin^2 4\theta)\Big]d\theta = \\ &= \frac{1}{16\pi}\mu(q,R)\int_{-\pi}^{\pi}\Big[(Q\mp iU) + (Q\pm iU)\cos 8\theta\Big]d\theta = \frac{1}{8}(Q\mp iU)\mu(q,R).\end{aligned} \tag{B.9}$$

Thus, the inverse Fourier transform of the angular component of ω_x^E is:

$$\begin{aligned}&\frac{1}{2\pi}e^{i4\xi}\int_0^\infty \tilde{\omega}_{x+4}^E(q)J_4(qr)qdq + \frac{1}{2\pi}e^{-i4\xi}\int_0^\infty \tilde{\omega}_{x-4}^E(q)J_{-4}(qr)qdq = \\ &\quad = \frac{1}{16\pi}\Big(e^{i4\xi}(Q-iU) + e^{-i4\xi}(Q+iU)\Big)\int_0^\infty \mu(q,R)J_4(qr)qdq = \\ &\quad\quad = \frac{1}{16\pi}(Q\cos 4\xi + U\sin 4\xi)\int_0^\infty \mu(q,R)J_4(qr)qdq,\end{aligned} \tag{B.10}$$

where the $J_{-n}(x) = (-1)^n J_n(x)$ property of Bessel functions has been used to state that $J_{-4}(x) = J_4(x)$.

Let us now compute the inverse Fourier transform of the angular component of the wavelet coefficient ω_y^E. The Fourier coefficients $\tilde{\omega}_{yn}^E(q)$ are:

$$\begin{aligned}\tilde{\omega}_{yn}^E(q) &= \frac{1}{8\pi}\mu(q,R)\int_{-\pi}^{\pi}\Big(Q\sin 4\theta - U\cos 4\theta\Big)e^{-in\theta}d\theta = \\ &= \frac{1}{8\pi}\mu(q,R)\int_{-\pi}^{\pi}\Big[Q\sin 4\theta(\cos n\theta - i\sin n\theta) - U\cos 4\theta(\cos n\theta - i\sin n\theta)\Big]d\theta = \\ &\quad = \frac{1}{8\pi}\mu(q,R)\int_{-\pi}^{\pi}\Big[-iQ\sin 4\theta\sin n\theta - U\cos 4\theta\cos n\theta)\Big]d\theta,\end{aligned} \tag{B.11}$$

and result in only the non-zero $n = \pm 4$ terms:

$$\tilde{\omega}^E_{y\pm4}(q) = \frac{1}{8\pi}\mu(q,R)\int_{-\pi}^{\pi}\Big[-U\cos^2 4\theta \mp iQ\sin^2 4\theta)\Big]d\theta = \\ = \frac{1}{16\pi}\mu(q,R)\int_{-\pi}^{\pi}\Big[(-U\mp iQ)+(-U\pm iQ)\cos 8\theta\Big]d\theta = \\ = \frac{1}{8}(-U\mp iQ)\mu(q,R). \tag{B.12}$$

The angular component of the wavelet coefficient ω_y^E then reads:

$$\frac{1}{2\pi}e^{i4\xi}\int_0^\infty \tilde{\omega}^E_{y+4}(q)J_4(qr)qdq + \frac{1}{2\pi}e^{-i4\xi}\int_0^\infty \tilde{\omega}^E_{y-4}(q)J_{-4}(qr)qdq = \\ = \frac{1}{16\pi}\Big(e^{i4\xi}(-U-iQ)+e^{-i4\xi}(-U+iQ)\Big)\int_0^\infty \mu(q,R)J_4(qr)qdq = \\ = \frac{1}{16\pi}(Q\sin 4\xi - U\cos 4\xi)\int_0^\infty \mu(q,R)J_4(qr)qdq \tag{B.13}$$

The last remaining step necessary to finally obtain the wavelet coefficients ω_x^E and ω_y^E is to solve the radial dependence of the angular components of ω_x^E and ω_y^E using equations (A.13) and (A.14). This time, the identification with (A.13) yields

$$\int_0^\infty \mu(q,R)J_4(qr)qdq = \frac{\sigma^2R^2}{4\pi^2}\int_0^\infty e^{-q^2(\sigma^2+R^2)/2}J_4(qr)qdq = \\ = \frac{\sigma^2R^2}{48\pi^2(\sigma^2+R^2)}\frac{r^4}{4(\sigma^2+R^2)^2}M\Big(3,5,-\frac{r^2}{2(\sigma^2+R^2)}\Big), \tag{B.14}$$

where the confluent hypergeometric function $M(3,5,z)$, expressed in terms of a generic variable z, is:

$$M(3,5,z) = \frac{\Gamma(5)}{\Gamma(3)\Gamma(2)}\int_0^1 e^{zu}u^2(1-z)du = 12\int_0^1 e^{zu}u^2(1-z)du. \tag{B.15}$$

Using the variable change $x = e^{zu}$, the integral above can be solved as follows:

$$M(3,5,z) = 12\int_0^1 e^{zu}u^2(1-z)du = \frac{12}{z^3}\int_1^{e^z}\Big(\ln^2 x - \frac{1}{z}\ln^3 x\Big)dx = \\ = \frac{12}{z^3}\Big|x(\ln^2 x - 2\ln x + 2) - \frac{x}{z}(\ln^3 x - 3\ln^2 x + 6\ln x - 6)\Big|_1^{e^z} = \\ = 12\frac{e^z\Big[z(z+4)+6\Big]-2(z+3)}{z^4}. \tag{B.16}$$

Combining now all the obtained results into equations (B.3) and (B.4), the wavelet coefficients ω_x^E and ω_y^E are:

$$\omega_x^E(r,\xi,\phi,R) = \frac{\sigma^2R^2}{16\pi^2(\sigma^2+R^2)}\Big[Qe^{-z}+(Q\cos 4\xi + U\sin 4\xi)\lambda(z,R)\Big], \\ \omega_y^E(r,\xi,\phi,R) = \frac{\sigma^2R^2}{16\pi^2(\sigma^2+R^2)}\Big[Ue^{-z}+(Q\sin 4\xi - U\cos 4\xi)\lambda(z,R)\Big], \tag{B.17}$$

with

$$\lambda(z,R) = \frac{1}{2\pi z^2}\Big[e^{-z}\Big(z(z+4)+6\Big)+2(z-3)\Big] \qquad z = \frac{r^2}{2(\sigma^2+R^2)}. \tag{B.18}$$

APPENDIX C

Attached code

As a complement to this written document, a directory containing some Python scripts implementing the application of the filter on point-like sources in simulations of the microwave sky, is included. The attached directory contains three executable scripts (*newCalibrationFunction.py*, *pointSourceGenerator.py* and *applyFilter.py*) illustrating the main proceedings done during this work, accompained by the calibration functions and tabulated errors necessary for their operation, organized in the following directories structure:

```
code/
    applyFilter.py
    config/
        B_phi_nside_1024_fw_3.333_dphi60_dR0.05.npy
        B_phi_nside_512_fw_5.5_dphi60_dR0.05.npy
        error_bar_p_B.npy
        ...
    newCalibrationFunction.py
    patches/
    pointSourceGenerator.py
```

For simplicity, since in this work we have only characterized the performance of the filter for our simulations of the 30 GHz, 100 GHz and 353 GHz Planck channels, and the $\sigma_{n,i}$ noise levels, the functionalities of the code are restricted to these scenarios, in which we can provide an estimation of the error associated to the determination of the polarization angle and intensity.

The libraries required to run the code, and a brief explanation of how to use each of the Python scripts, and the outputs they produce, will be addressed in the following sections.

C.1 Language and libraries

The designed filter is implemented in Python 3.6. The fundamental libraries supporting the code implementation are the *numpy*, *scipy*, *astropy* and *matplotlib* libraries. To work in the sphere, the *healpy*[1] library (the Python version of the HEALPix [17] pixelization) is also needed. Finally, simulations of the

[1] Available for download at the official website: https://healpix.sourceforge.io/

microwave sky are generated using the *Python Sky Model* [28] software, through the *pysm*[2] library.

The attached code was only tested in a Unix operative system, so some conflict may arise if the code were to be executed in a Windows operative system.

C.2 *newCalibrationFunction.py*

This script computes the calibration functions, $f^{E,B}$ and $g^{E,B}$, needed to correct the pixelization induced effects hindering the determination of the polarization angle and intensity. As previously explained in section 2.3, the calibration functions are calculated through equations 2.31 using the initial outputs for polarization intensity and angle the filter returns when applied to a naked source. To run the script, the user only has to specify the combination of FWHM/pix ratio and nside parameter describing the sphere's pixelization for which calibration functions should be calculated. Optionally, the user can also change the steps controling the angles and filter scales for which the calibration function will be tabulated. The *help* message produced by *newCalibrationFunction.py* is here shown as a user guide:

```
usage: newCalibrationFunction.py [-h] [-r dR/sigma] [-a dphi] [-v]
                                 fwhmpix NSIDE

newCalibrationFunction
----------------------

Computes calibration functions for both polarization intensity and angle
for new combinations of nside and FWHM/pix ratios.
Default : dphi=1 degree dR/sigma=0.05.

positional arguments:
  fwhmpix       Size of the FWHM of the Gaussian PSF in number of pixels.
                Several can be run as: "fwhm1 fwhm2 fwhm3 ... "
  NSIDE         HEALPIX NSIDE parameter describing sphere pixelization.
                 Several can be run as: "NSIDE1 NSIDE2 NSIDE3 ... "

optional arguments:
  -h, --help    show this help message and exit
  -r dR/sigma   Step in the R/sigma filter scales used to construct the
                function. Default=0.05
  -a dphi       Step in the angles used to construct the function.
                 Default=1 degree
  -v            Verbose mode. Default = False
```

The outputs produced by *newCalibrationFunction.py* are stored in the *config* directory, in the form of *.npy numpy* binary files. For every pair of input FWHM/pix, x, and nside, y, values, files "*B phi nside y fw x dphi60 dR0.05.npy*", "*B p nside y fw x dphi60 dR0.05.npy*" and "*phi B nside y fw x dphi60 dR0.05.npy*" (and their counterparts for the E-modes) are produced. These files contain, respectively, the angle calibration function, the intensity calibration function, and the initial angles $\hat{\phi}^{E,B}$ returned by the

[2] Available for download at the public repository provided by its authors: https://github.com/bthorne93/PySM_public

filter. The calibration functions used during this project are already stored in the *config* directory.

C.3 *pointSourceGenerator.py*

The purpose of this script is the preparation of the projected patches of the sky containing the point-like sources where the filter will be applied. The user can choose the frequency channel, the instrumental noise, and the properties (position in the sky, flux, polarization degree and polarization angle) of the point-like source to simulate. Only the 30 GHz, 100 GHz and 353 GHz channels, and the $\sigma_{n,i}$ noise levels are allowed as inputs so far. The produced E- and B-mode patches will be stored in the *patches* directory, inside a subdirectory with the name passed in the *patch_name* parameter like: *patch_name_E.npy* and *patch_name_B.npy*. When running the script, several sources can be simulated at once, being all of them stored simultaneously in the same *_E.npy* and *_B.npy* files. The proper order to state the different properties of the point-like sources is specified in the following *help* message:

```
usage: pointSourceGenerator.py [-h] [-p coordinates] [-v]
                               frequency patch_name position flux
                               polarization_degree polarization_angle
                               noise_level

pointSourceGenerator
--------------------

Returns a flat patch of the E- and B-mode polarization maps of the microwave
sky, with a point-like source of the desired properties at its center. Only
the 30 GHz, 100 GHz and 353 GHz channels of the Planck satellite, and the
three noise levels defined in the work are simulated.

positional arguments:
  frequency             Frequency (GHz) of the Planck channel to simulate.
  patch_name            Name for the output patches.
  position              Introduce source coordinates as: 'theta1,phi1
                        theta1,phi1...'.
  flux                  Flux (Jy) for the point-like source. Introduce
                        as:'flux1 flux2 ...'. polarization_degree  Polarization degree
  polarization_angle    Polarization angle of each source in degrees.
  noise_level           Index indentifying the three noise levels used in the
                        work. 1 is the highest and 3 is the lowest.

optional arguments:
  -h, --help            show this help message and exit
  -p coordinates        Format for the input source coordinates: longitude and
                        latitude ('lonlat') or spherical theta and phi
                        ('thetaphi'). Default=thetaphi
  -v                    Verbose mode. Default = False
```

This script reflects the process followed during this work to simulate point-like sources. Firstly, the intensity and Stokes' parameters Q and U polarization maps of the microwave sky simulating the selected frequency channel are generated. After transforming these Q and U maps into E- and B-mode maps, a $12.8^\circ \times 12.8^\circ$ region centered at the selected position, is projected onto the plane. Is in this patch where a point-like source of the desired properties, analytically computed through equations (2.5), is added. To overcome the different conventions present in definitions in the plane and in the sphere, and make the computed profiles compatible, a phenomenological factor multiplying polarization intensity is added in the code. The precise relation between these definitions still has to be addressed. Lastly, the white Gaussian noise characterized by the choosen $\sigma_{n,i}$ is also added to the patch.

C.4 *applyFilter.py*

applyFilter.py operates on the output patches produced by *pointSourceGenerator.py*, and, in order to run, needs the calibration functions and tabulated errors contained in the *config* directory. This script applies the filter to the chosen pair of *patch_name_E.npy* and *patch_name_B.npy* files stored in the *patches* directory, printing in the terminal the obtained polarization angles and intensities, with their associated errors. The input *patch_name* is the same used for *pointSourceGenerator.py*, without adding any additional indications. However, the script allows for the use of calibration functions of different precisions, so the user must type the full name of the calibration function, as the *help* message specifies:

```
usage: applyFilter.py [-h] [-v]
                      patch_name frequency calibration_function_name
                      noise_level

applyFilter
_____________

Applies the filter to the given patches and returns the polarization angle
(degrees) and intensity (Jy), with their associated errors.

positional arguments:
  patch_name            Name for the input patches.
  frequency             Frequency (GHz) channel the patches come from.
  calibration_function_name
                        Name for the calibration function in .npy format. For
                        example:"nside 512 fw 5.5 dphi60 dR0.05"
  noise_level           Index indentifying the three noise levels used in the
                        work. 1 is the highest and 3 is the lowest.

optional arguments:
  -h, --help            show this help message and exit
  -v                    Verbose mode. Default = False
```

In the script, the Fourier transform of the input maps is multiplied by an image of the filter (computed directly in Fourier space). The wavelet coefficients are then obtained through the inverse Fourier transform

of such product. From the wavelet coeffiecients, an estimation of the polarization angle and intensity of the source is computed using the equations previously described in section 2.2. Finally, in order to determine which error to associate to the returned values of the polarization angle and intensity, the dispersion of the patch (σ_{patch}) is calculated. Attending to the definition of the different regions of the sky, presented in section 2.4, and considering how the instrumental noise ($\sigma_{n,i}$) affects the dispersion the patch would have had before its addition ($\sigma^2_{patch} = \sigma^2_{before} + \sigma^2_{n,i}$), we can determine which cell in table 2.5 describes the situation at hand. Since we count with no extra information about the polarization intensity of the source, we give the largest error tabulated for each noise level in said table.